

Ministry of Education and Science of the Russian Federation
FEDERAL STATE-FUNDED EDUCATIONAL
INSTITUTION OF HIGHER EDUCATION
“SAINT PETERSBURG NATIONAL RESEARCH UNIVERSITY OF
INFORMATION TECHNOLOGIES, MECHANICS AND OPTICS”
Faculty of Physics and Engineering

Department of Nanophotonics and Metamaterials

Pavel Alekseevich Dmitriev

Resonant Optical Properties of Crystalline Dielectric Nanoparticles, Fabricated by Laser Ablation-Based Methods

Master’s Thesis

12.04.03 — Photonics and Optoinformatics

Admitted for defence.
Head of the chair:
D. Sc. P. A. Belov

Scientific supervisor:
Dr. A. K. Samusev

Saint-Petersburg
2017

Contents

Introduction	8
1. Dielectric Nanophotonics	9
1.1. Crystalline Silicon as the Material of Choice for Dielectric Nanophotonics	9
1.2. Analytical Models	9
1.2.1. Mie-Type Resonances of Dielectric Nanoparticles	9
1.2.2. Raman Scattering from Crystalline Materials	10
1.3. Numerical Models	11
1.3.1. Discrete Dipole Approximation	11
1.3.2. Finite Element Method	11
1.3.3. Finite Difference Time Domain	12
1.3.4. Finite Integration Technique	12
1.4. Fabrication of Dielectric Nanoparticles	12
1.4.1. Chemical Synthesis	12
1.4.2. Thin-Film Dewetting	13
1.4.3. Laser Ablation-Based Methods	13
1.4.4. Lithographic Methods	13
1.5. Experimental Characterization Methods	13
1.5.1. Electron Microscopy	13
1.5.1.1. Transmission Electron Microscopy	14
1.5.1.2. Scanning Electron Microscopy	14
1.5.2. Optical Characterization	14
1.5.2.1. Elastic Scattering — Dark-field Microscopy	15
1.5.2.2. Inelastic Scattering — Raman Scattering	15
1.5.3. Scanning Probe Methods	15
1.6. Goals	16
2. Methods	17
2.1. Fabrication of Crystalline Silicon Nanoparticles by Femtosecond Laser Ablation	17
2.1.1. Laser Writing of Dielectric Particles	17
2.1.2. Laser Transfer of Crystalline Dielectric Particles	18
2.2. Optical Measurements	19
2.2.1. Polarization-Resolved Dark-field Spectroscopy of Single Nanoparticles	19
2.2.2. Raman Spectroscopy of Single Nanoparticles	19
2.3. Analytical Model of Raman Signal Enhancement by Mie Resonances	20
2.3.1. Numerical Methods	23
2.3.2. Discrete Dipole Approximation	24

2.3.3. Finite Integration Technique	24
3. Experimental Results	25
3.1. Fabrication of Crystalline Silicon Nanoparticles	25
3.1.1. Laser Writing of Nanoparticles	25
3.1.2. Laser Transfer of Nanoparticles	25
3.2. Characterization of Resonant Optical Modes of the Nanoparticles	27
3.3. Determining Size of Nanoparticle from Optical Resonance Positions	28
3.4. Raman Scattering Enhancement from Single Nanoparticles	29
Results	32
Approbation of Work	34
Appendices	35
Appendix A. Mie Scattering of Light	35
A.1. Maxwell's Equations	35
A.2. Scalar Solution	36
A.3. Vector Solution	37
A.4. Incident, Scattered and Internal Fields	38
A.5. Mie Coefficients	39
A.6. Cross Sections	40
Appendix B. Raman Scattering from Crystalline Materials	42
Appendix C. Femtosecond Laser Ablation	44
C.1. Generation of femtosecond laser pulses	44
C.2. Ultrashort-pulse laser ablation	44
Appendix D. Discrete Dipole Approximation	46
Appendix E. Finite Integration Technique	50
References	55

Introduction

Nanophotonics is a field that studies light manipulation at the nanoscale — using various nanostructures to control the propagation of light. Nanophotonic devices can range from relatively simple perfect reflectors/absorbers to optical computers. Applications include antireflective coatings for solar cells, all-optical switching for optical telecommunications, and various medical sensing tasks.

Traditionally, nanophotonic devices have utilized plasmonic nanostructures. Plasmonic metallic nanoparticles have strong electric dipole resonances, meaning that they readily interact with the electric component of electromagnetic fields. Problems arise when one tries to control the magnetic component of electromagnetic fields, because plasmonic nanoparticles do not have an inherent magnetic dipole response. A solution is the split-ring resonator — a nanostructure with both electric and magnetic dipole resonances. Having building blocks to control both the electric and magnetic components of electromagnetic fields, plasmonic structures have been efficiently used in frequency ranges from gigahertz to several hundred terahertz — up to infrared wavelengths. But, because of strong losses in the optical spectral range, and of the complexity of fabricating split-ring resonators for optical wavelengths, plasmonics have had a lot of difficulty in achieving the required performance for optical nanophotonic devices [1].

Mie theory [2] predicts and it has been experimentally demonstrated [3] that high-index dielectric nanoparticles have both electric and magnetic resonances. The positions of the resonances are size and shape dependent, making them easily tunable for any wavelength. Crystalline silicon has proven itself as a good material for dielectric nanophotonics — low losses at optical wavelengths [4], high refractive index, and compatibility with many fabrication processes [5, 6, 7, 8, 9, 10, 11, 1].

Dielectric nanoparticles have been used for sensing and electromagnetic field enhancement [12, 13, 14, 15], antireflective coatings [16], perfect reflectors [7, 17], light wavefront manipulation [18, 19], superdirective scattering [20, 21] and enhancement of nonlinear effects [22, 23].

1. Dielectric Nanophotonics

1.1 Crystalline Silicon as the Material of Choice for Dielectric Nanophotonics

Crystalline silicon has been almost ubiquitously chosen as the material of choice for dielectric nanophotonics. There are several reasons for this. First, the material parameters are suitable for visible and infrared nanophotonic devices — Crystalline silicon has a high refractive index, $n \approx 3.5$ at visible and IR wavelengths [24], giving high contrast with air, and therefore good field confinement for resonant particles at those wavelengths [2, 25]. Also a very important fact, distinguishing crystalline silicon from amorphous silicon, is the near zero absorption at visible wavelengths, meaning that crystalline silicon nanoparticles are nearly lossless at visible and IR wavelengths, making any potential nanophotonic devices very efficient and not prone to thermal dissipation — something that plagues their plasmonic counterparts. Silicon, being the basis of almost all modern electronics, can easily boast a highly developed ecosystem of fabrication and processing technologies, making it very easy (if expensive) to fabricate almost any required structure. Last, but not least, silicon is a bio-compatible material, meaning it is easy to design nanophotonic devices for medical applications.

Another interesting application dimension is related to the existence of and intrinsic Raman response in crystalline silicon. Raman scattering of light, and inelastic scattering phenomenon, is an important electromagnetic effect [26] that has a large number of applications: sensing [27], optical amplification [28], lasing [29]. Traditionally, enhancement of Raman scattering for SERS applications has been mostly delegated to metallic nanoparticles, but recent studies of high-index subwavelength nanoparticles have paved the way for all-dielectric resonant nanophotonic devices, including the possibility of enhancing Raman scattering, including intrinsic Raman from the nanoparticles.

1.2 Analytical Models

1.2.1 Mie-Type Resonances of Dielectric Nanoparticles

An important problem for dielectric nanophotonics is the scattering of electromagnetic radiation by a homogeneous sphere. This problem has an analytical solution, generally called Mie theory [2]. The solution of this problem utilizes the symmetry of the problem, and decomposes the scattered radiation into vector spherical harmonics. The result is a set of coefficients, a_i, b_i describing the relative contributions of a_i , electric multipole resonances and b_i , magnetic multipole resonances into the final scattered field.

Based on this, one can easily estimate the extinction, scattering and absorption cross-sections (for a detailed derivation, see Appendix A):

$$C_{sca} = \frac{2\pi}{k_m^2} \sum_{l=1}^{\infty} (2l+1)(|a_l|^2 + |b_l|^2) \quad (1)$$

$$C_{ext} = \frac{2\pi}{k_m^2} \Re \sum_{l=1}^{\infty} (2l+1)(a_l + b_l) \quad (2)$$

$$C_{abs} = C_{ext} - C_{sca} \quad (3)$$

The main limitation of the Mie solutions is their reliance on the symmetry of the scatterer — the solution can be generalized to layered spheres, layered infinite cylinders, but scatterers lacking symmetry cannot be accurately described by Mie-type solutions. In those cases, T-Matrix methods can be used, but they are outside the scope of this thesis.

1.2.2 Raman Scattering from Crystalline Materials

Raman scattering of light from crystalline materials is inelastic scattering resulting from the interaction of optical phonons with the incident light. Raman scattering is a versatile method of probing the phonon structure of the materials. A simplistic classical model of Raman scattering is sufficient to demonstrate the effect and to properly predict many of the Raman scattering peaks of semiconductors [30]. In the model, interaction between light and phonons is represented as a perturbation of the electric susceptibility χ :

$$\chi(\vec{k}_i, \omega_i, \vec{Q}) = \chi_0(\vec{k}_i, \omega_i) + \frac{\partial \chi}{\partial \vec{Q}_0} \vec{Q}(\vec{r}, t) + \dots \quad (4)$$

Where Q represents the displacement of atoms in the lattice by phonons. Then the induced polarization by the incident light, perturbed by the phonons can be written as

$$\vec{P}_{ind}(\vec{r}, t, \vec{Q}) = \frac{\partial \chi}{\partial \vec{Q}_0} \vec{Q}(\vec{r}, t) \vec{F}_i(\vec{k}_i, \omega_i) \cos(\vec{k}_i \cdot \vec{r} - \omega_i t) \quad (5)$$

which contains both Stokes and anti-Stokes shifted components. The intensity of the Raman scattered light is dependent on the polarization of the incident light and the phonon structure of the material. All of this information can be condensed into a second rank Raman tensor:

$$\hat{R} = \frac{\partial \chi}{\partial \vec{Q}} \vec{Q}_n \quad (6)$$

$$I_s \propto |\vec{e}_i \cdot \hat{R} \cdot \vec{e}_s|^2 \quad (7)$$

A more detailed derivation can be found in Appendix B.

1.3 Numerical Models

Since scattering from arbitrarily-shaped particles cannot be analytically described, use of numerical modeling methods is required to model these particles. A large number of numerical methods exist that can be used for these purposes.

1.3.1 Discrete Dipole Approximation

The discrete dipole approximation (DDA) is a method of numerically simulating light scattering from arbitrarily shaped particles. The general idea of the method is to replace an arbitrarily shaped scatterer by a set of point dipoles and calculate the scattering by each dipole on its own plus the interaction between the dipoles. This makes calculations straightforward for scatterers of arbitrary geometries and compositions. Using this assumption, the extinction and absorption cross-section are represented by simple sums, iterating over all of the point dipoles, using the polarization of each dipole and the field at the location of the dipole [31]:

$$C_{abs} = 4\pi k \sum_i V_i \Im(\chi_i) |\vec{E}_i|^2 = 4\pi k \sum_i \Im(\vec{P}_i \vec{E}_i^*) \quad (8)$$

$$C_{ext} = 4\pi k \sum_i \Im(\vec{P}_i \cdot \vec{E}_i^{inc*}) \quad (9)$$

The main disadvantage of this method is staircase errors, caused by based approximation of ellipsoidal boundaries by a point-dipole model on a Cartesian grid. The only real solution is to increase the number of dipoles used to simulate the scatterer, which quickly increases computation time. Another difficulty is including surface interaction, which adds another interaction term to the solution, and further complicates the computation. A detailed derivation of the basic DDA is provided in Appendix D.

1.3.2 Finite Element Method

The Finite Element Method (FEM) is a numerical technique, first introduced in the 1940s [32], to find approximate solutions to boundary-value problems. The technique has been used in many fields, from mechanical structure problems to electromagnetic field propagation. The idea of the method is to replace a continuous domain by a number of sub-domains, in each of which the solution is approximated by interpolation functions. A linear system of algebraic equations is obtained by applying continuity boundary conditions on the internal sub-domains and problem-specific boundary conditions on the external sub-domains. The system can then be solved by any solver for linear systems. The subdomains are generally chosen to be tetrahedra or hexahedra for three-dimensional solutions with the internal fields approximated by piecewise polynomial functions, but, in general, the method has no limitations on the shape and size of the subdomains and the approximation functions inside each of the subdomains. This allows the method to accurately model complicated scattering geometries. The flip side of this flexibility —

large space requirements for the system of equations. The method also often requires iterative refinement of the grid to achieve good convergence.

1.3.3 Finite Difference Time Domain

The Finite Difference Time Domain (FDTD) method is very straightforward technique to solve the propagation of electromagnetic radiation, first developed by Yee [33]. The method approximates both spatial and temporal derivatives in the Maxwell's equations by finite-difference expressions. The standard implementation does this on a staggered Cartesian grid, with the electric field defined on one sub-grid and the magnetic field defined on the second sub-grid. This results in a system of linear equations, where each time step is used to calculate the electric field on the first sub-grid from the magnetic field on the second sub-grid, and then the magnetic field at the next time step from the electric field, and so on, until a termination condition is reached. The main advantage of this method is its simplicity — no matrix solvers required, possibility for very efficient implementations. The disadvantage is that this simplicity makes the method very rigid in terms of time step and spatial step choices for good convergence, to mitigate staircase-type errors caused by inefficient mapping of complex scatterer geometry onto a Cartesian grid.

1.3.4 Finite Integration Technique

The Finite Integration Technique (FIT) [34], is ideologically similar to the FDTD method, but works with the integral formulation of Maxwell's equations instead of the derivative formulation used by the FDTD. This grants the method more flexibility in grid geometry, allowing for more accurate modeling of complicated scatters. The accuracy of the method, like with FDTD, is still highly dependent on the choice of grid size and time step. A detailed derivation for a simplistic case, with a Cartesian grid, can be found in Appendix E.

1.4 Fabrication of Dielectric Nanoparticles

There are several techniques to fabricate dielectric nanoparticles. They can be ordered in terms of level of control over the size of the particles and the options of building patterned nanostructures for the nanoparticles. Complexity and cost of the processes generally correlate with the level of control provided by the different techniques. The main techniques can be grouped into: chemical synthesis [35], thin-film dewetting [36], laser ablation-based [37] and lithographic methods.

1.4.1 Chemical Synthesis

Chemical vapor deposition of silicon from disilane gas has been used to fabricate silicon nanoparticles, ($Si_2H_6 \rightarrow 2Si + 3H_2$ at high temperatures) yielding polycrystalline spherical particles [35]. Monodisperse colloidal particles have been fabricated from trisilane (Si_3H_8) at high temperature in n-Hexane [38]. In that study, the sizes of the particles were controlled by varying the concentration of trisilane and the temperature of the reaction. The main disadvantages of these types of methods are the

porosity and high hydrogen concentration of the particles and necessity of further processing if ordered nanostructures are required.

1.4.2 Thin-Film Dewetting

Thermal dewetting of thin films can be used to create arrays of nanoparticles, with size and phase controlled by the thickness of the initial film and temperature of the process [36]. If fabricated from an unpatterned film, the particles will be unordered — producing ordered particles in this way requires an additional patterning of the film, usually by lithographic processes, which increases the complexity of the process and the cost.

1.4.3 Laser Ablation-Based Methods

Laser ablation by focused ultra-short pulses can also be used to fabricate nanoparticles by heating up the irradiated area to eject material into spherical particles deposited either near the irradiated area [3] or transferred to another substrate [37]. Control of the beam spot, fluency and donor material structure can be used to control individual particle size and the number of particles fabricated from a single pulse (down to one particle in best-case scenario). The ultra-short pulses can also be used to change the phase of already fabricated structures by means of light-induced thermal annealing. The main advantage of femtosecond laser ablation is the ability to gently remove material from the surface — allowing for very precise and controllable modification of the surface or precise and controllable formation of nanoparticles. Femtosecond laser ablation is a complicated process that requires complex 3D simulations to accurately predict the outcome of the light-material interaction. A simple qualitative description is provided in Appendix C

The shortcomings of the current methods are that they often require additional annealing to crystallize the fabricated nanoparticles and that method presented in Ref. [37] is limited to transferring nanoparticles to transparent substrates.

1.4.4 Lithographic Methods

Using electron beam lithography and reactive ion etching, one can pattern substrates with high-quality nanocylinders, with near-perfect control of both size and positioning of the structures [14]. This gives great flexibility in terms of fabricating ordered nanostructures, but at the cost of extreme process complexity.

1.5 Experimental Characterization Methods

1.5.1 Electron Microscopy

Electron microscopy is a very high-resolution, down to single nanometer resolutions, group of methods to probe geometrical and material parameters of structures. The structure is probed by a focused

electron beam, measuring either scattered or transmitted primary electrons, secondary electrons or emitted photons. Because of charge accumulation caused by the electron beam, samples usually need to be conductive to facilitate charge draining, or else the resulting signal will be distorted. The two main methods used are scanning electron microscopy (SEM) and transmission electron microscopy (TEM).

1.5.1.1 Transmission Electron Microscopy

In TEM, a collimated high-voltage electron beam, is used to illuminate the specimen. The transmitted beam is then projected, with magnification, onto a viewing screen. The transmitted electron beam contains information on the material properties of the sample, based on the interaction of the electrons in the beam with the sample.

This type of microscopy can achieve sub-nanometer resolutions, and can be used to probe different phases of materials, see different grains of polycrystalline materials and even visualize crystalline defects such as dislocations.

The main difficulty related to TEM is the complicated sample preparation — good TEM samples should be around 100nm thick, for optimal electron-sample interaction.

1.5.1.2 Scanning Electron Microscopy

In SEM, a focused electron beam illuminates a small portion of the sample, and the image of the sample is formed by collecting either back-scattered electrons, secondary electron, Auger electrons or characteristic X-Rays. Depending on what signal is collected, different information about the sample is obtained, e.g. different types of signals originate from different interaction volumes, giving differing information of about bulk or surface sample composition.

Secondary electrons originate from within a few nanometers of the surface, giving good topographical information.

Backscattered electrons also give information about chemical composition, since heavier elements backscatter electrons more strongly, with those areas appearing brighter in the final image.

1.5.2 Optical Characterization

The scattering properties of nanostructures (in the visible spectral range) can be measured by relatively simple optical measurements. A very good method for measuring elastic scattering is dark-field microscopy, where the only collected signal is the light scattered by the structure. Inelastic scattering often means either Fluorescence measurement or Raman scattering. More involved, nonlinear, effects, for example, second and third harmonic generation, can also be put in the same inelastic scattering category, but are outside the scope of this thesis. In the first shorter wavelength light is absorbed by the sample and then re-emitted as longer wavelength light, usually with rather large shifts in wavelength, making measurements relatively easy. Raman scattering, on the other hand, is usually much weaker than the excitation signal, and spectrally very close to the excitation signal, making it relatively difficult to single out.

1.5.2.1 Elastic Scattering — Dark-field Microscopy

Dark-field microscopy has the excitation source angled to the surface of the sample substrate in such a way, that none of the reflected excitation illumination can enter the collection channel. In terms of objective numerical apertures this means that the excitation source is at an angle larger than the critical angle of the collection channel objective. The only light that is collected by the collection objective is light scattered from the sample. This allows for direct measurement of the scattering properties of the sample. A schematic of such a system can be seen in Fig. 2 in the next chapter.

This is usually used to measure elastic scattering — the collected scattered light is the same wavelength as the excitation.

1.5.2.2 Inelastic Scattering — Raman Scattering

Fluorescence microscopy and Raman scattering involve measuring scattered light at a wavelength that is different from the wavelength of the excitation. This generally requires filtering out the excitation wavelengths, and is especially important for Raman measurements, where the wavelength shift between the excitation and scattered is very small. A schematic of such a system can be seen in Fig. 2 in the next chapter.

1.5.3 Scanning Probe Methods

Another class of characterization methods exist that can probe the geometrical and electromagnetic properties of nanostructures. These include techniques like atomic force microscopy (AFM) to probe geometrical properties and near-field scanning optical microscopy (NSOM), which can be used to probe electromagnetic field modes close to the structures.

1.6 Goals

The project was devoted to the fabrication as well as the study of resonant optical properties of silicon nanoparticles via elastic and inelastic scattering.

The goals of this project were to:

- Implement the Discrete Dipole Approximation method to calculate scattering cross-sections of dielectric particles
- Develop a simple, single-stage femtosecond laser ablation method of fabricating crystalline silicon nanoparticles
- Carry out optical characterization through single-particle polarization-resolved scattering experiments
- Determine the sizes of the particles based on the spectral positions of the Mie-type resonances of the particles
- Perform single-particle Raman spectroscopy experiments to prove crystallinity
- Study the influence of Mie resonances on Raman scattering from particles.

2. Methods

2.1 Fabrication of Crystalline Silicon Nanoparticles by Femtosecond Laser Ablation

The first part of the project was to develop a new, simple, method of fabricating crystalline dielectric nanoparticles. The idea was to use controlled laser ablation — a very simple technique — to produce the particles. Previous work on the topic [3, 37] has shown that it is possible to fabricate single particles of a certain size.

We ended up developing two different methods to fabricate crystalline nanoparticles — direct laser writing of crystalline nanoparticles out of a thin film of amorphous silicon (adapted from a method used for plasmonic nanoparticles [39, 40]), and a forward transfer of nanoparticles by single femtosecond laser pulses from a transparent substrate with a thin film of amorphous silicon to an arbitrary acceptor substrate. The second method is similar to the one presented in Ref. [37], but does not require any additional annealing steps to achieve nanoparticle crystallinity and is not limited to transparent acceptor substrates.

The femtosecond laser system used for this project, Femtosecond Oscillator TiF-100F by Avesta Project, is a Ti:Sapphire laser pumped by a Nd:YLF frequency doubled laser, emitting laser pulses at a central wavelength of 800 nm, with pulse duration of 100 fs, and repetition frequency of 80 MHz.

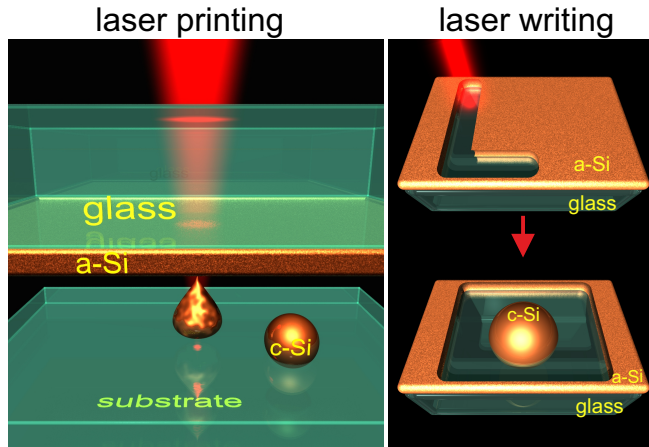


Figure 1: Geometry of laser-ablation based fabrication methods of crystalline nanoparticles from amorphous thin films.

2.1.1 Laser Writing of Dielectric Particles

Laser writing of crystalline silicon nanoparticles was done directly in an initially amorphous thin film of a-Si:H. The film was patterned by a train of femtosecond pulses — by ablating the directly irradiated material, one can cut patches out of the a-Si film [39, 40]. The area irradiated by a single laser pulse with a fluence of $F \approx 100 \text{ mJ/cm}^2$ is brought close to the melting point of silicon, while using a pulse train with

a delay of 12.5 ns between the pulses causes heat accumulation in the film, reaching and exceeding the ablation threshold. Heat is also transferred to the non-irradiated areas of the film, and tends to accumulate in the cut-out patches, because they are thermally isolated from the rest of the film, and the thermal conductivity of the substrate is much lower than the thermal conductivity of the film. These patches become unstable at high temperatures and can dewet to form a number of nanoparticles [41]. The size and number of the resulting nanoparticles can be controlled by laser fluence and repetition rate, cut patch size, and initial film thickness.

2.1.2 Laser Transfer of Crystalline Dielectric Particles

Laser transfer of the nanoparticles was carried out using single femtosecond laser pulses. The particles were fabricated from a thin, amorphous, a-Si:H film in a forward transfer geometry (the relieving substrate is below the donor substrate and film, with a spacing of around $\sim 50 \mu\text{m}$ — see Fig. 1(a)). All of the particles were fabricated from previously undamaged areas of the silicon thin film. A forward-transfer geometry has an advantage over the back-transfer geometry that was presented in Ref. [37] — it does not force the substrate to be transparent, allowing particles to be transferred to a wide variety of substrates, including structured, opaque samples.

The single laser pulses required for the technique were selected from a train of femtosecond laser pulses by a Pockels cell pulse picker from Avesta Project. The pulses were focused by an $100\times$ Olympus oil immersion microscope objective with a numerical aperture of $NA = 1.4$. Using the Rayleigh criterion, $d \approx 1.22\lambda/NA$ the beam's focal spot size can be estimated to be $d = 0.7 \mu\text{m}$, which is closer to the value estimated by a method using the dependence of the area damaged by the laser on the laser energy ($0.68 \mu\text{m}$) [42].

The film used for the fabrication process was an 80 nm thick a-Si:H film deposited on a fused silica substrate by plasma enhanced chemical vapor deposition (PECVD) from a SiH₃ precursor gas. Laser energies in the range of 0.5 – 1.2 nJ, were used in the fabrication process, providing fluencies in the range of 0.12 – 0.16 J/cm². The fabricated nanoparticles were close to being spherical in shape (figure 8(b)) and with diameters in the range of 50 – 200 nm, depending on the fluence.

2.2 Optical Measurements

All of the optical characterization measurements were carried out on a multifunctional setup, depicted in Fig. 2. The setup allowed us to measure optical signals from single nanoparticles, provided that there was at least $1\mu\text{m}$ between the nanoparticle and its nearest neighbors. The XYZ-stage used for the positioning of the particles had 100nm precision, giving enough control to position a single nanoparticle into the center of the excitation beam.

The scattered light was collected from the top by an objective (Mitutoyo M Plan APO NIR, 100x, NA=0.7), sent to a Horiba LabRam HR spectrometer and projected onto a thermoelectrically cooled charge-coupled device (CCD, Andor DU 420A-OE 325) with a 150-g/mm diffraction grating. The spectrometer gave us a spectral resolution of around 1nm.

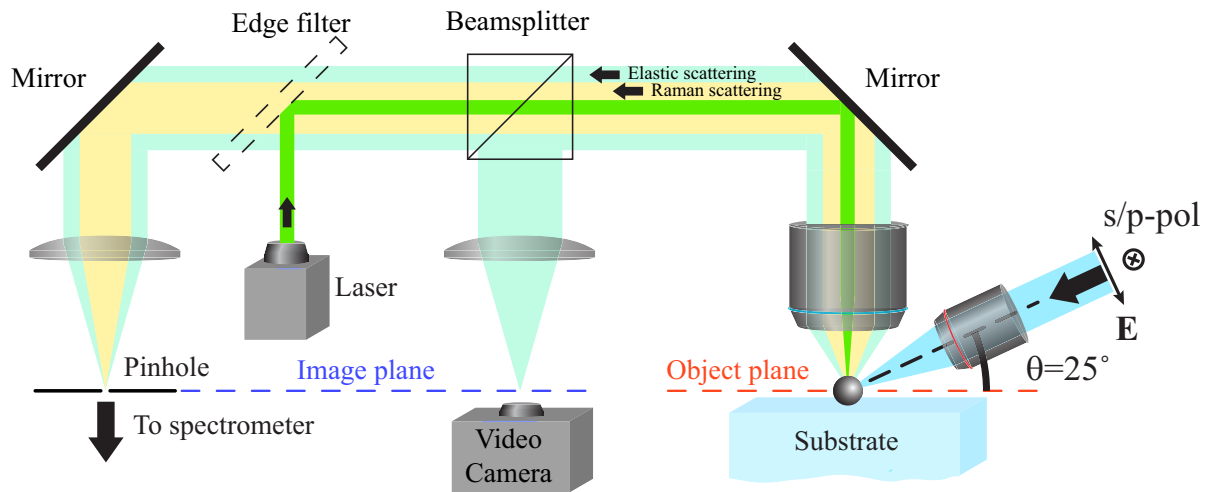


Figure 2: Schematic of the experimental setup used for all of the optical measurements.

2.2.1 Polarization-Resolved Dark-field Spectroscopy of Single Nanoparticles

For the dark-field scattering experiments, the nanoparticles were excited at an oblique angle of incidence (65 degrees to the surface normal) by linearly polarized light from a halogen lamp (HL-2000-FHSA) through a weakly-focusing objective (Mitutoyo M Plan Apo NIR, 10x, NA=0.28). The polarization allowed us to selectively excite different modes in the nanoparticles [43], see Fig. 3.

2.2.2 Raman Spectroscopy of Single Nanoparticles

For the Raman scattering experiments, the nanoparticles were excited by one of two laser sources: a 632.8nm HeNe laser or a 532nm Nd:YAG laser, through the same channel that was used to collect the scattered light. A lowpass filter was used to filter out the excitation wavelength and leave only the Stokes-shifted inelastically scattered light.

Raman intensity is proportional to the volume of the Raman-active material. One of the goals of the project was to compare the intensity of Raman scattering by particles with different resonance positions,

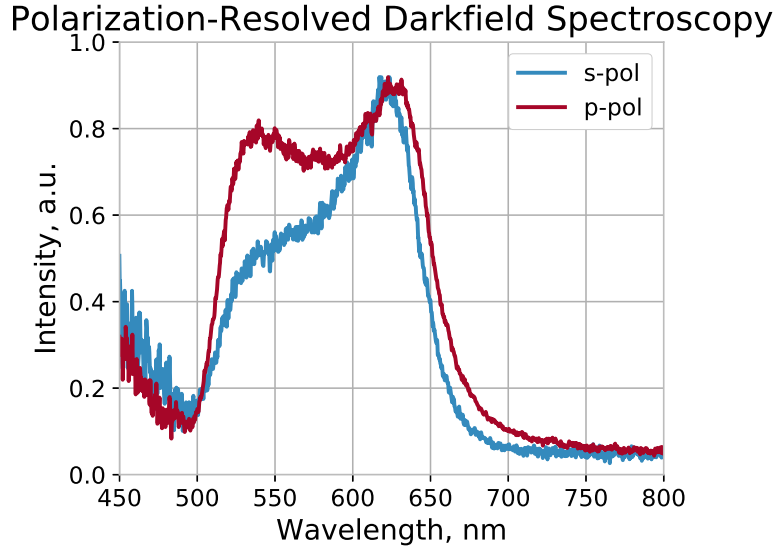


Figure 3: Different Mie-type resonances excited by different polarizations of incident light.

which meant comparing particles of different sizes. This meant that for any meaningful comparison, the Raman signal had to be normalized to the volume of the particles, allowing comparisons of intensity per volume to be made.

2.3 Analytical Model of Raman Signal Enhancement by Mie Resonances

This derivation is taken from the derivation in Ref. [25].

The rigorous Green tensor approach was used to describe the role of the electric and magnetic Mie resonances in the enhancement of Raman scattering of a silicon nanoparticle. The theoretical approach is based on earlier related studies [44, 45].

The first was to determine the spatial distribution of the electric field $\mathbf{E}_{exc}(\mathbf{r})$ at the excitation frequency inside the nanoparticle from an external source. Assuming a spherical particle, in free space, with illumination by a plane wave, the normalized electric field inside the nanoparticle can be decomposed into a series of vector spherical harmonics [46]:

$$\mathbf{E}_{exc}(\mathbf{r}) = \sum_{n=1}^{\infty} E_n \left(c_n \mathbf{M}_{o1n}^{(1)}(\mathbf{r}) - id_n \mathbf{N}_{e1n}^{(1)}(\mathbf{r}) \right), \quad (10)$$

where c_n and d_n are Mie coefficients, $\mathbf{M}_{o1n}^{(1)}$ and $\mathbf{N}_{e1n}^{(1)}$ — orthogonal vectorial spherical harmonics, and $E_n = i^n(2n+1)/[n(n+1)]$. The distribution of the excitation electric field at each point inside the nanoparticles defines the Raman polarization oscillating the Stokes-shifted frequency ω_S :

$$\mathbf{P}_s(\mathbf{r}) = \chi_s \hat{\alpha}_j(\mathbf{r}) \mathbf{E}_{exc}(\mathbf{r}), \quad (11)$$

where χ_s is the scalar Raman susceptibility, $\hat{\alpha}_j$ is the Raman polarizability tensor representing the three-

fold degenerate transverse optical (TO) phonon mode excitation [47, 30].

The induced Raman polarization, then produces an electromagnetic field at an observation point \mathbf{r}_0 :

$$\mathbf{E}_s(\mathbf{r}_0) = (\omega_s^2/c^2) \int_V \hat{G}_s(\mathbf{r}_0, \mathbf{r}) \mathbf{P}_s(\mathbf{r}) d^3\mathbf{r} \quad (12)$$

where $\hat{G}_s(\mathbf{r}_0, \mathbf{r})$ is the Green tensor at the Stokes-shifted frequency, accounting for the Si nanoparticle. The integration is carried out over V , the volume of the nanoparticle. Then, the resulting signal at \mathbf{r}_0 can be written as:

$$S(\mathbf{r}_0) = \sum_j \langle \mathbf{E}_s^*(\mathbf{r}_0) \mathbf{E}_s(\mathbf{r}_0) \rangle = \sum_j \frac{\omega_s^4}{c^4} \iint_V d^3\mathbf{r}_1 d^3\mathbf{r}_2 \left\langle \hat{G}_s^*(\mathbf{r}_0, \mathbf{r}_1) \mathbf{P}_s^*(\mathbf{r}_1) \hat{G}_s(\mathbf{r}_0, \mathbf{r}_2) \mathbf{P}_s(\mathbf{r}_2) \right\rangle \quad (13)$$

$$= \sum_j \frac{\omega_s^4}{c^4} \iint_V d^3\mathbf{r}_1 d^3\mathbf{r}_2 \hat{G}_s^*(\mathbf{r}_0, \mathbf{r}_1) \mathbf{E}_{exc}^*(\mathbf{r}_1) \hat{G}_s(\mathbf{r}_0, \mathbf{r}_2) \mathbf{E}_{exc}(\mathbf{r}_2) \chi_s^2 \langle \hat{\alpha}_j^*(\mathbf{r}_1) \otimes \hat{\alpha}_j(\mathbf{r}_2) \rangle, \quad (14)$$

the summation is performed over the three degenerate TO phonon modes of silicon. Raman scattering is a spontaneous process (unless we are in the stimulated Raman scattering regime), meaning that the induced polarization \mathbf{P}_s is not coherent across the particle. To account for that, the averaging in Eq. (14) is carried out over all possible orientations of Raman polarization \mathbf{P}_s . Because the correlation length of Raman scattering in silicon, L_c , is much less than the nanoparticle diameter (for particles resonant in the visible and near-infrared spectral ranges), being on the order of tens of nanometers, it is possible to approximate the correlation of the Raman by the Dirac delta function:

$$\langle \hat{\alpha}_j(\mathbf{r}_1) \otimes \hat{\alpha}_j(\mathbf{r}_2) \rangle \sim \delta(\mathbf{r}_1 - \mathbf{r}_2) \quad (15)$$

This reduces Eq. (14) to

$$S(\mathbf{r}_0) = \frac{\omega_s^4}{c^4} \sum_j \int_V d^3\mathbf{r} \left| \hat{G}_s(\mathbf{r}_0, \mathbf{r}) \hat{\alpha}_j \chi_s \mathbf{E}_{exc}(\mathbf{r}) \right|^2 \quad (16)$$

Eq. 16 can be simplified by the single-mode approximation, which is applicable in this case, because the electromagnetic response of an optically small particle is always dominated by a single multipole resonance [7]. Because of this, only one term from Eq. 10 is required to describe the electric field inside the nanoparticle:

$$\mathbf{E}_{exc} \approx E_n c_n \mathbf{M}_{o1n}^{(1)} \quad (17)$$

$$\mathbf{E}_{exc} \approx -i E_n d_n \mathbf{N}_{e1n}^{(1)} \quad (18)$$

For the n -th magnetic or n -th electric resonance.

Because the Raman shift in silicon, compared to the linewidth γ of Mie resonances at ω_0 , is small, the main contribution to the Green tensor is also provided by the same Mie resonance of the particle.

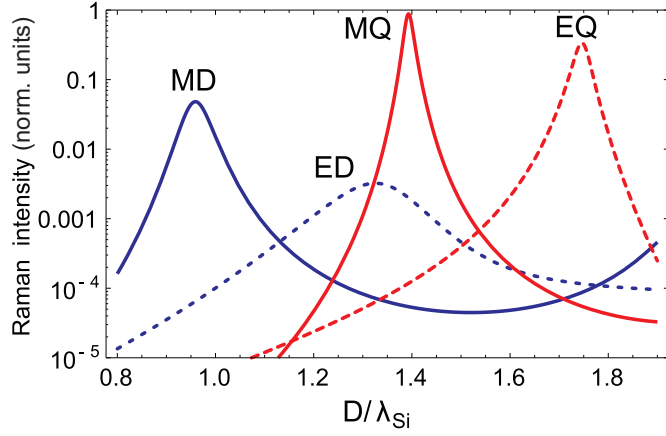


Figure 4: Log plot of normalized intensity of Raman scattering as a function of dimensionless nanoparticle diameter for the magnetic dipole (MD), electric dipole (ED), magnetic quadrupole (MQ) and electric quadrupole (EQ) resonances.

Expanding the Green tensor in a series of eigenmodes [48] and discarding all terms except the resonant one:

$$\hat{G}_s(\mathbf{r}_0, \mathbf{r}) \approx \frac{c^2}{N^2} \frac{\mathbf{u}(\mathbf{r}_0) \otimes \mathbf{u}^*(\mathbf{r})}{(\omega_0 + i\gamma)^2 - \omega_s^2}, \quad (19)$$

where $\mathbf{u}(\mathbf{r})$ is the spatial distribution of the field of the eigenmode, $N^2 = \int \text{Re}\epsilon(\mathbf{r}) |\mathbf{u}(\mathbf{r})|^2 d^3\mathbf{r}$ is a normalization constant. After integrating Eq. 19 over the volume V of the nanoparticle, an expression for Raman signal enhanced by a single Mie resonance, can be written:

$$S(\mathbf{r}_0) \approx V \left(\frac{\omega_s}{c} \right)^4 \left| \frac{\chi_s s_n}{(\omega_0 + i\gamma)^2 - \omega_s^2} \right|^2, \quad (20)$$

where s_n stands for the Mie coefficient — either c_n or d_n , electric or magnetic, of the mode. The equation shows that enhancement of Raman scattering depends on two main factors: enhancement of the excitation field inside the medium, and the Purcell enhancement of the Raman dipole radiation [49]. Two main parameters in Eq. (20) are resonance frequency ω_0 and linewidth γ . The first can be easily estimated numerically, and the second can be estimated by an analytical expression from Ref. [50]. Using these values, The spectrum of Raman enhancement by different resonances of a spherical silicon nanoparticle can be plotted. Assuming a constant excitation wavelength of 633 nm (used in the Raman scattering experiments in this thesis), which corresponds to a wavelength of $\lambda_{\text{Si}} = 163$ nm inside the nanoparticle, the spectrum, normalized to particle volume $V = 4\pi R^3/3$, is plotted in Fig. 4 as a function of dimensionless nanoparticle diameter D/λ_{Si} . The spectrum shows the contributions of the magnetic dipole (MD), electric dipole (ED), magnetic quadrupole (MQ) and electric quadrupole (EQ) resonances.

Eq. 20, being a single-mode expression, can be used to easily decompose the total Raman scattering enhancement into the constituent Mie resonance components. Fig. 4 clearly shows, that the strongest enhancement is caused by the magnetic quadrupole resonance (MQ), owing to its high $Q - factor$. Another interesting fact is that the strongest Raman enhancement is caused by magnetic resonances, with

both magnetic quadrupole (MQ) and dipole (MD) resonances out-performing their electric counterparts, EQ and ED, with MD being more than an order stronger than ED.

2.3.1 Numerical Methods

Several numerical methods were used to simulate the scattering properties of the fabricated nanoparticles — to prove their crystalline phase, to probe their shape, to determine their size. The initial idea was to use the Discrete Dipole Approximation, because it is very flexible and can work with scatterers of arbitrary geometry. The main problem that was encountered was the fact the method is very involved (especially if one tries to incorporate substrate interaction), and computationally intensive for the required problems. Many calculations turned out to be excessive – a simple Mie theory calculation, while simulating a slightly different geometry, was more than enough to model the required parameters, with error well within the requirements.

For calculations of field distribution inside the nanoparticles presented in this thesis, CST Microwave Studio was used. It is an EM simulation package that uses the Finite Integration Technique for most of its calculations.

2.3.2 Discrete Dipole Approximation

For the DDA calculations, a custom, Python-based implementation was written, PyDDA — a reimplementation of an existing Matlab toolkit, DDA-SI [51]. The implementation even included surface-interaction components in its' calculations, but the complexity of the calculation and difficulty of accurately modeling particles led to the DDA being abandoned in favor of plain Mie theory, which provided more than enough accuracy for the purposes of the project.

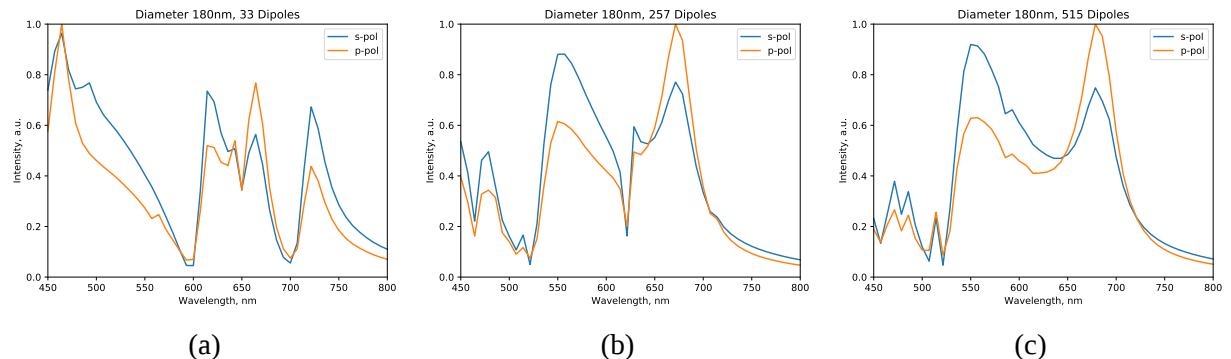


Figure 5: Scattering from isotropic sphere modeled by DDA using a) 33, b) 257, c) 515 dipoles to model the sphere.

2.3.3 Finite Integration Technique

CST Microwave studio was used to model field distribution inside and around the silicon nanoparticles, to demonstrate the electric field confinement at different types of resonances (electric and magnetic dipole resonances). The model was a slightly oblate spheroid, corresponding to the experimentally determined geometric parameters of the nanoparticles.

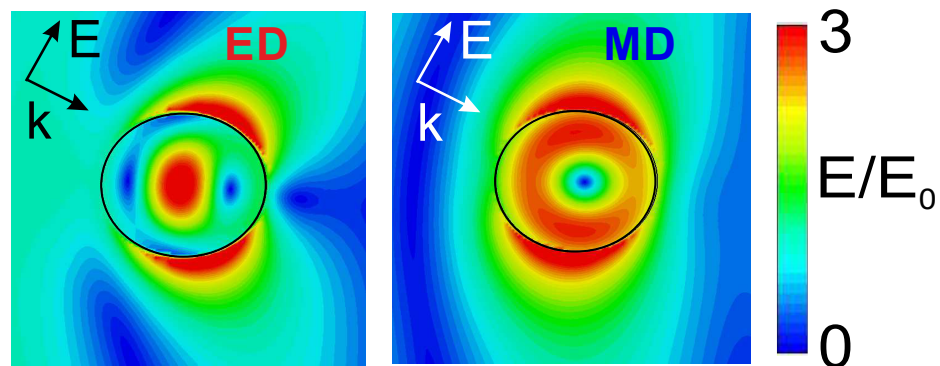


Figure 6: Field distribution inside 180nm spheroid nanoparticle with 1.12 oblateness parameter at electric and magnetic dipole resonances, calculated using CST Microwave Studio

3. Experimental Results

3.1 Fabrication of Crystalline Silicon Nanoparticles

3.1.1 Laser Writing of Nanoparticles

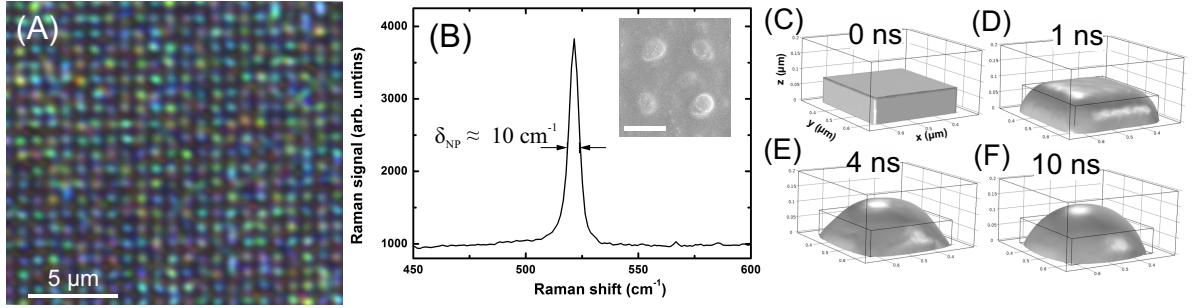


Figure 7: A. Dark-field image of array of nanoparticles fabricated by direct laser writing. B. Raman peak of single nanoparticle. Inset - SEM image of several nanoparticles. C-F. COMSOL Model of transformation of liquid silicon patch into hemisphere.

Under the optimal conditions of fabrication, the method described in Sec. 2.1.1 can create and ordered array of nanoparticles, with a period of $0.9 \mu\text{m}$. Dark-field imaging of the arrays show that the nanoparticles exhibit bright colors, which indicates resonant scattering — see Fig. 7A. The cutting process produces square patches, but the resulting arrays are arrays of nearly circular nanoparticles, as can be seen on SEM images — see Fig. 7B. This is caused by the dewetting of the thermally isolated patches into hemispherical particles, caused be heat accumulation and overheating during the cutting process. COMSOL Simulations of a square liquid silicon patch with a side of 300 nm and height of 80 nm on a substrate of fused silica, solving the incompressible Navier-Stokes equations with realistic models of the materials show, that after about ten nanoseconds, the the initial patch has transformed into an hemisphere with an approximate height and width of 140 nm and 350 nm — see Figs. 7C-F. This is in good qualitative agreement with the experimentally observed nanoparticles.

Measurement of Raman signals from these nanoparticles shows that the particles are, indeed, crystalline — they demonstrate a narrow peak at 520 cm^{-1} , with a half-width of about 10 cm^{-1} (Fig. 7B). This half-width correspond to average crystallite sizes of less than 10 nm, according to previous studies [52].

3.1.2 Laser Transfer of Nanoparticles

The initial a-Si:H film, used for the fabrication of the nanoparticles was amorphous, a fact supported by its broad Raman peak, centered at 480 cm^{-1} . In contrast to the Raman signal of the initial film, the Raman signal from the individual nanoparticles, fabricated using the laser transfer method described in Sec. 2.1.2, had narrow peaks centered at 521.5 cm^{-1} , which is very close to the reference Raman signal from a bulk crystalline silicon wafer, centered at 520 cm^{-1} . The slight positive shift of the position of the

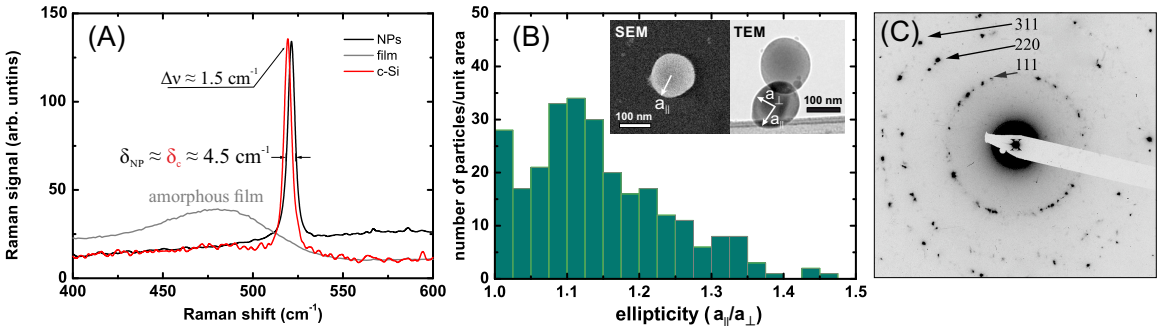


Figure 8: A. Raman signal from (gray) initial amorphous film, (red) bulk crystalline silicon, (black) single nanoparticle, fabricated by laser transfer. B. Histogram of ellipticity of nanoparticles; insets — SEM and TEM images of nanoparticles. C. Electron diffraction pattern from cluster of nanoparticles.

Raman peak from the nanoparticles, $\Delta\nu = 1.5 \text{ cm}^{-1}$, can be explained by residual compressive stress [53] in the nanoparticles, from the transfer process from donor to acceptor substrate. Similar to the previous method, by measuring the half-width of the Raman peak of the nanoparticles, around $4\text{--}5 \text{ cm}^{-1}$, one can estimate the minimum crystallite size, which, in this case is larger than $\sim 20 \text{ nm}$, because the Raman peaks of the nanoparticles have almost the same half-width as the peak from a bulk crystalline silicon wafer (4.5 cm^{-1}) [52].

The Raman measurements are supported with electron diffraction patterns of clusters of the printed nanoparticles. The fabricated nanoparticles were deposited on transmission electron microscopy specimen grids (3-mm-diameter, 200-mesh copper grids, coated on one side with a 20-nm-thick film of amorphous carbon). Using TEM, along with electron diffraction to demonstrate the crystallinity, the size and shape and composition of the nanoparticles were studied, using bright and dark-field TEM imaging, see Fig. 8B. The electron diffraction pattern from a cluster of nanoparticles shows a number of clear maxima, which correspond to several crystalline planes of silicon (Fig. 8C). Because the specimen grids were even, the particles were deposited at different angles to the substrate, allowing their shapes to be studied from the TEM images — providing information on the particles' oblateness. The average ellipticity of the particles, $a_{\parallel}/a_{\perp} \approx 1.12$, where $a_{\parallel}(a_{\perp})$ is the particle semi-major (semi-minor) axis oriented parallel (perpendicular) to the surface of the substrate. Scanning electron microscopy, (SEM, using a Carl Zeiss Neon 40), of particles deposited on a flat, even substrate, confirm that the particles possess axial symmetry along the substrate normal (Fig. 8B). These results correlate with previously observed ellipticity of the printed silicon nanoparticles [37].

Previous studies of femtosecond laser ablation as a method of fabricating silicon nanoparticles [37, 54] have shown that the average size of the fabricated nanoparticles is determined by the laser fluence used. Experiments carried out as part of this thesis also showed similar behavior. The experiments demonstrated two distinct regimes of nanoparticle fabrication. The first regime, observed at fluencies of up to 150 mJ/cm^2 , has nanoparticle size proportional to the laser fluence, which can be seen in Fig. 9A–C as a change in color from blue to red. This can be explained by the spallation mechanism of laser ablation, where a thin molten layer is spalled due to the laser-induced tensile pressure waves [55, 56], breaking

into a number of liquid droplets via the Rayleigh-Plateau instability [57]. The photomechanically spalled volume increases as $V \sim \ln(E)$ when illuminated by a Gaussian beam, because of the logarithmic dependence of the spalled surface layer area $r_s^2 \sim \ln(E)$ [58], while the thickness of the layer remains almost constant [55] or even slightly decreases [56]. Previous studies of nanoparticle fabrication from crystalline silicon an increase of the molten volume led to an increase in the number [54] and size [37] of fabricated nanoparticles, which agrees with current results (Fig. 9A–C).

The second regime of nanoparticle fabrication is observed at fluencies over 150 mJ/cm^2 , generating large (red) and small nanoparticles at the same time, with a broad size distribution — see Fig. 9D. This regime is caused by the unstable boiling of superheated silicon [59, 55, 56]. In this regime, nanoparticles are formed by explosive decomposition of material into small droplets and vapor [60, 56], which result in nanoparticles with average sizes less than 100 nm [61]. This regime has been extensively studied [61, 62] for biomedical applications. The high-fluence regime (Fig. 9D) does not produce monodisperse, reproducible nanoparticles, unlike the low low-fluence regimes (Fig. 9A–C). This makes the low-fluence regimes more desirable for controllable nanoparticle fabrication and deposition onto acceptor substrates. Raman, TEM and SEM characterization of the printed silicon nanoparticles were used to quantify their crystalline phase, proving that it is possible to controllably fabricate crystalline silicon nanoparticles from amorphous films with a single stage process.

3.2 Characterization of Resonant Optical Modes of the Nanoparticles

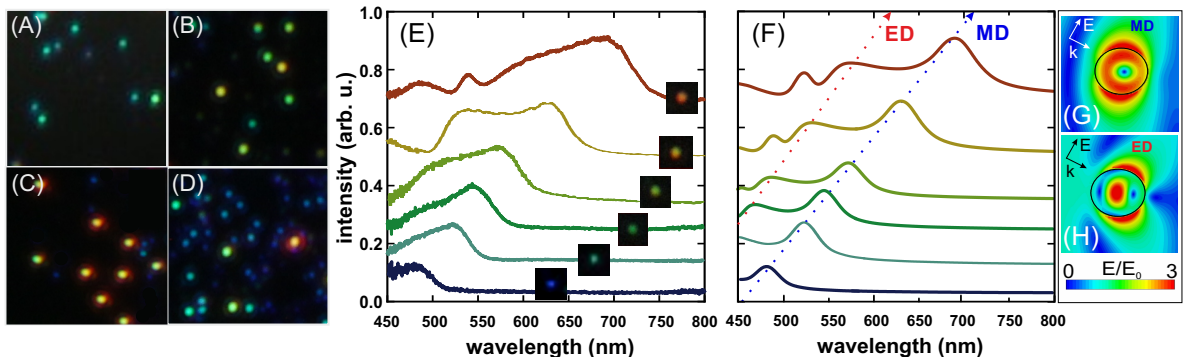


Figure 9: Dark-field optical images of silicon nanoparticles fabricated at different peak fluencies: 120 (A), 130 (B), 140 (C), 160 mJ/cm^2 (D). Experimental (E) and theoretical (F) spectra for scattered p-polarized incident light (angle of incidence is 65°) from individual nanoparticles with the radius parallel to substrate surface $a_{\parallel} = 55 \text{ nm}$ (blue), 65 nm (spring green), 68 nm (green), 72 nm (olive), 85 nm (yellow) and 92 nm (red) with the ellipticity coefficient of 1.12. Numerically calculated electric field distributions in the silicon nanoparticle with $a_{\perp} = 85 \text{ nm}$ the wavelengths of 635 nm (G) and 525 nm (H).

Dark-field scattering measurements showed that the nanoparticles posses a number of resonances, corresponding to different Mie-type resonances, see Fig. 9. To determine which resonances correspond to electric dipole (ED) and magnetic dipole (MD) resonances, the scattering properties of and electric field distribution near and inside the nanoparticles were modeling using the FIT technique in CST Microwave

Studio.

The scattering geometry was modeled as a c-Si ellipsoid with different axis (a_{\perp} and $a_{||}$) and the fixed ellipticity $a_{||}/a_{\perp} \approx 1.12$, i.e. for the most probable ellipticity parameter in the experiments. The ellipsoid was irradiated by a plane wave at the angle 65° in vacuum, modeling the geometry used in the dark-field scattering experiments. Substrate effects were deemed to be insignificant, which is justified in the next section. The optical properties for c-Si were taken from Ref. [63]. Modeling of scattering spectra (Fig. 9F) showed good agreement with the corresponding experimental ones (Fig. 9E), whereas the modeled electric field distributions in the ellipsoids at different wavelengths proved the excitation of MD (Fig. 9G) and ED (Fig. 9H).

3.3 Determining Size of Nanoparticle from Optical Resonance Positions

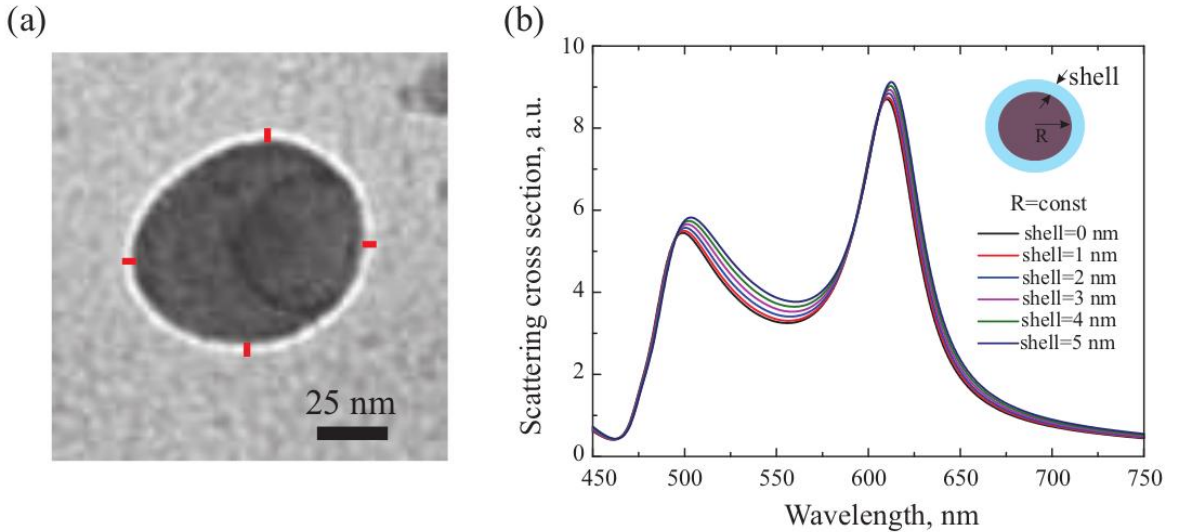


Figure 10: **a.** TEM image of the typical silicon nanoparticle fabricated using laser-induced forward transfer technique. Red lines represent 5 nm. **b.** Total scattering cross sections of silicon nanoparticle ($R = 75$ nm) coated with silica layers with different thicknesses.

Resonant optical properties of silicon nanoparticles are known to be sensitive to their shape [64], crystallinity [64, 65], to the substrate [66] and to the thickness of native oxide layer [64, 11], which is always present on silicon surface [67]. The shape of the particles was characterized using SEM and TEM measurements, while the diameter of silicon core has been extracted from dark-field spectroscopy experiments, by comparing the positions of the experimental resonances to those of Mie resonators of different sizes.

Additional experimental measurements and numerical simulations were done to analyze the influence of native silicon oxide layer on the optical properties of the studied nanoparticles. The average thickness of the native oxide layer was estimated by transmission electron microscopy (TEM) of a typical silicon nanoparticle, see Fig. 10A. The measurements showed that nanoparticles are coated with a thin layer of

SiO_2 , at most 5-nm-thick, which agrees with previous results [64, 11]. To analyze the influence of the oxide layer on the resonant properties of nanoparticles, total scattering cross section spectra of a crystalline silicon nanoparticle ($D = 150 \text{ nm}$) surrounded by silica shells with different thicknesses were simulated, see Fig. 10. For the sake of simplicity, the simulations have been carried out using Mie theory [46]. The results of the simulations confirm that in the case of a fixed silicon core diameter, the appearance of an additional 5-nm-thick silica layer leads to red spectral shifts of both electric and magnetic dipole resonances of the nanoparticle at most by $\approx 4.2\text{nm}$ and $\approx 2.5\text{nm}$. The influence of different substrates has been analyzed in Ref. [66] The authors have demonstrated that both electric and magnetic dipole resonances of crystalline silicon nanoparticle placed on the fused silica substrate exhibit small red spectral shifts with respect to the resonances of the nanoparticle in free space. In the case of nanoparticle with the diameter of $D = 130\text{nm}$ these shifts are around $\approx 3.5\text{nm}$ and $\approx 0.5 \text{ nm}$. Therefore, the spectral shift of the nanoparticle's magnetic dipole resonance is almost insensitive to both the substrate and the native silica layer. This allows for accurate estimation of the the diameter of silicon core of the nanoparticle from the spectral position of magnetic dipole resonance in the dark-field spectroscopy measurements by comparing to the simulations based on Mie theory.

3.4 Raman Scattering Enhancement from Single Nanoparticles

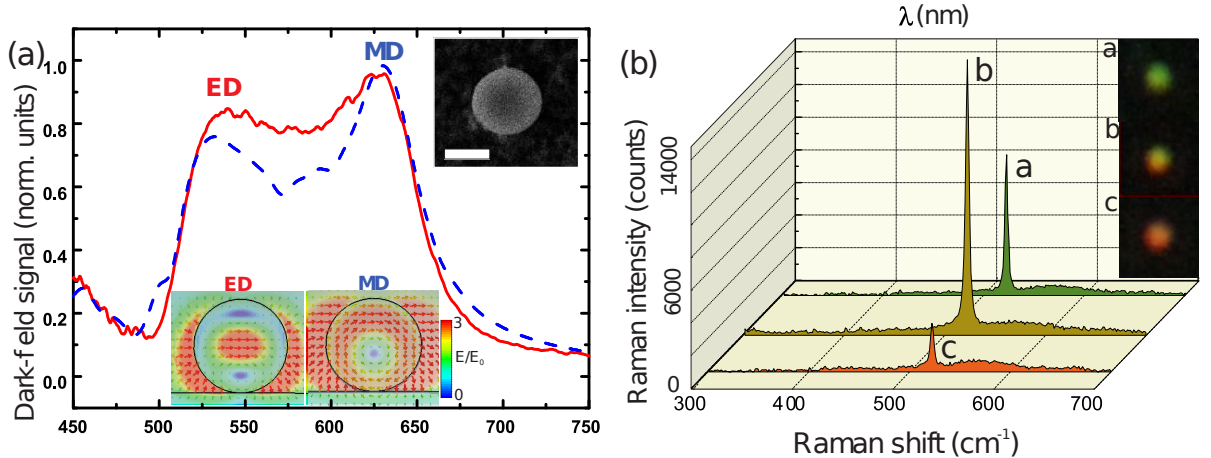


Figure 11: (a) Experimental (solid) and theoretical (dashed) scattering spectra for s-polarized incident light. Bottom inset: the electric field distribution at different wavelengths, corresponding to electric dipole (ED) and magnetic dipole (MD) resonances. Upper inset: SEM image of typical ablative c-Si nanoparticle (scale bar represents 100 nm). (b) Raman spectra for different nanoparticles at the excitation wavelength of 633 nm and the corresponding dark-field optical images of the nanoparticles: (a) $D=153 \text{ nm}$, (b) $D=158 \text{ nm}$, (c) $D=173 \text{ nm}$.

Theoretically predicted Raman scattering enhancement on different Mie-type resonances, see Sec. 2.3 was demonstrated experimentally be measuring Raman scattering from single crystalline nanoparticles, fabricated using the laser transfer process described in Sec. 2.1.2. During the Raman measurements it was noted that different nanoparticles exhibit different intensities of Raman scattering, and that that intensity

of the scattering has a non-trivial dependence on particle size, see Fig. 11b. For the excitation wavelength of $\lambda=633$ nm, the maximum Raman intensity corresponds to particles with a diameter $D \approx 155$ nm, which corresponds to a magnetic dipole (MD) resonance at the excitation wavelength. To be able to compare different Raman measurements among themselves they needed to be normalized, because Raman scattering is dependent on the volume of the excited Raman-active medium. To calculate enhancement factors, a baseline intensity also needed to be chosen. A non-resonant particle, e.g. with diameter $D \approx 135$ nm, demonstrating the smallest measured Raman signal, was chosen as the baseline intensity, relative to which the enhancement factor was calculated. The enhancement factor, EF, was calculated according to the formula $EF = (I/I_{\text{norm}}) \times (V/V_{\text{norm}})$, where I is Raman scattering signal from a studied nanoparticle with known diameter and volume V , I_{norm} is Raman signal from a nanoparticle of known volume V_{norm} chosen as the baseline, in this case, a nanoparticle with the smallest Raman signal. The maximum value of the enhancement factor (EF) for nanoparticles with a MD resonance at 633nm was calculated to be $EF \approx 140$.

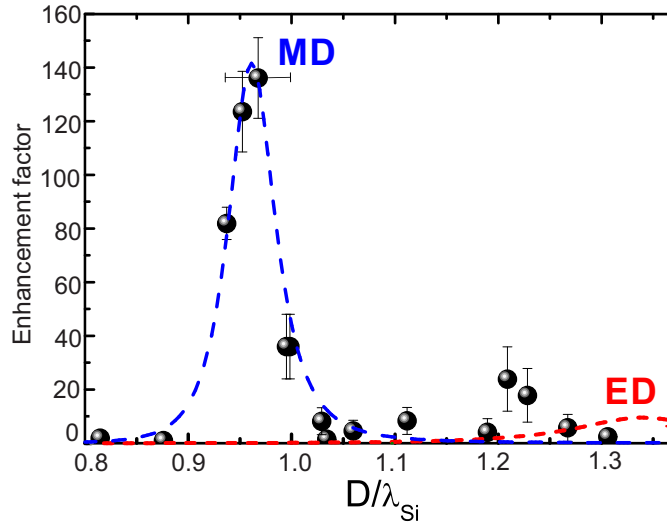


Figure 12: Theoretical (dashed curves) and experimental (black dots) dependencies of the enhancement factor for Raman scattering from spherical silicon nanoparticles on their diameter D normalized to the excitation wavelength in silicon. Theoretical dependence consists of two contributions from magnetic dipole (blue dashed curve) and electric dipole (red dashed curve).

In order to compare the experimental enhancement factors to the predicted contributions from different resonances, the enhancement factor of Raman scattering needed to be plotted relative to the dimensionless particle size D/λ_{Si} , taking into account the dispersion of the refractive index of silicon. The result of this is show on Fig. 12. The resulting dependence has a pronounced peak at $D/\lambda_{\text{Si}} \approx 1$, with $EF \approx 140$ i.e. near the magnetic dipole resonance, which agrees with the theoretical prediction from Sec. 2.3. This maximum EF is about 5-7 times larger than the EF for the electric dipole. Insets in Fig. 11a, showing the confinement of the electric field at the ED and MD resonances provide an illustrative interpretation of this enhancement. The MD resonance confines a larger fraction of the electric field inside the nanoparticle than the ED resonance, therefore producing more efficient excitation of the Raman active medium and

thus increasing total Raman polarization and emission. The theoretical predictions, for perfect spherical nanoparticles, have an even larger difference in EF between ED and MD resonances (~ 10), which is not achieved in experiment because of nanoscale imperfections in the nanoparticles and the existence of a thin native oxide layer [11, 64]. The results shown in Fig. 12 are limited to nanoparticle diameters $D/\lambda_{\text{Si}} < 1.3$ because the fabrication method is limited in the maximum size of produced nanoparticles without significant deviations from a spherical shape. Even a small deviation from the spherical leads to suppression of the MQ resonance [11], which makes large but aspherical particles applicable to only study enhancement on ED and MD resonances.

Results

Two methods of fabricating crystalline nanoparticles, based on femtosecond laser ablation, nanoparticles were developed. A direct laser-writing technique, allowing for precise patterning of a substrate (coated with a thin film of α -Si), where a train of femto-second laser pulses is used to pattern a thin film of α -Si — cutting it into isolated patches of silicon, which dewet into nanoparticles from the absorbed heat from the pulses. With precise optimization of the thickness of the film, the laser fluence and pulse frequency, it is possible to create ordered arrays of nearly identical nanoparticles. The second technique, forward transfer of nanoparticles by single femtosecond laser pulses from an amorphous thin film onto a acceptor substrate, is more flexible — particle diameter can be controlled in the range of 100 – 200nm by adjusting the fluence of the laser pulses, there is virtually no limitation on the type of acceptor substrate, i.e. almost anything can be coated by crystalline nanoparticles. Both methods produce crystalline nanoparticles in a single-step process, making the fabrication methods very simple and potentially high throughput.

It has also been shown, both theoretically and experimentally, that Raman scattering from the crystalline silicon nanoparticles can be enhanced by the Mie-type modes of the nanoparticles. This happens when the wavelength of the excitation source corresponds to the wavelength of a Mie resonance of the nanoparticle. The enhancement happens because of field confinement inside the nanoparticle, leading to more efficient excitation of the Raman-active volume of crystalline silicon. The strongest enhancement has been shown to be from magnetic resonances, because of the strong field confinement inside the particle and high Q factor of the resonance. 140-fold increase in Raman scattering from resonant particles, enhanced on the magnetic dipole resonance has been demonstrated.

The main results of the project can be summarized as follows:

1. Two methods for single-stage fabrication of crystalline silicon nanoparticles using femto-second laser ablation were developed:
 - Direct laser writing of arrays of nanoparticles in an amorphous silicon thin-film;
 - Forward laser transfer of crystalline nanoparticles from amorphous silicon thin-films to arbitrary substrates.
2. The crystallinity of the nanoparticles was confirmed by electron diffraction and Raman measurements.
3. The implemented DDA model was applied for apspherical nanoparticles. The shape-dependent shifts of resonances obtained from the model were compared to pure Mie-theory and FIT modeling.
4. The elasting scattering of light from nanoparticles was measured in a dark-field configuration.
5. The obtained spectral positions of Mie-type resonances allowed to estimate sizes of nanoparticles.
6. Measurements of Raman scattering intensity from crystalline nanoparticles were carried out.
7. It was shown the Raman signal intensity demosntrates resonant behaviour with change of relative positions of excitation wavelength and Mie-type resonances of the nanoparticles.

Approbation of Work

1. Dmitriev PA, Makarov SV, Milichko VA et al. Laser fabrication of crystalline silicon nanoresonators from an amorphous film for low-loss all-dielectric nanophotonics // *Nanoscale*. — 2016. — Vol. 8, no. 9. — P. 5043–5048.
2. Dmitriev Pavel A, Baranov Denis G, Milichko Valentin A et al. Resonant Raman scattering from silicon nanoparticles enhanced by magnetic response // *Nanoscale*. — 2016. — Vol. 8, no. 18. — P. 9721–9726.
3. Dmitriev PA, Makarov SV, Milichko VA et al. Direct Femtosecond Laser Writing of Optical Nanoresonators // *Journal of Physics: Conference Series* / IOP Publishing. — Vol. 690. — 2016. — P. 012021.
4. Dmitriev P, Baranov D, Makarov S et al. Femtosecond laser transfer of silicon nanoparticles with enhanced Raman response // *AIP Conference Proceedings* / AIP Publishing. — Vol. 1748. — 2016. — P. 030001.
5. Dmitriev PA, Makarov SV, Milichko VA et al. Single-stage fabrication of low-loss dielectric nanoresonators from high-loss material // *Journal of Physics: Conference Series* / IOP Publishing. — Vol. 690. — 2016. — P. 012020.

Appendices

Appendix A Mie Scattering of Light

An important problem for dielectric nanophotonics is the scattering of electromagnetic radiation by a homogeneous sphere. This problem has an analytical solution, generally called Mie theory [2]. The following is a condensed version of the solution, following the presentation from Ref. [68]. We will assume an x-polarized incident wave with amplitude E_0 , propagation constant β_0 traveling in the z direction:

$$\vec{E}_{inc} = E_0 e^{i\beta_0 z} \hat{x} \quad (21)$$

A.1 Maxwell's Equations

Starting with

$$\nabla \times \vec{E} = i\omega\mu\vec{H} \quad (22)$$

$$\nabla \times \vec{H} = -i\omega\epsilon\vec{E} \quad (23)$$

Taking the rotor of the equations and substituting,

$$\nabla \times (\nabla \times \vec{E}) = i\omega\mu\nabla\vec{H} = \omega^2\epsilon\mu\vec{E} \quad (24)$$

$$\nabla \times (\nabla \times \vec{H}) = i\omega\epsilon\nabla\vec{E} = \omega^2\epsilon\mu\vec{H} \quad (25)$$

Applying the vector identity,

$$\nabla \times \nabla \vec{A} = \nabla(\nabla \cdot \vec{A}) - \nabla \cdot (\nabla \vec{A}) \quad (26)$$

We get the following wave equations

$$\nabla^2 \vec{E} + k_m^2 \vec{E} = 0 \quad (27)$$

$$\nabla^2 \vec{H} + k_m^2 \vec{H} = 0 \quad (28)$$

$$k_m^2 = \omega^2\epsilon\mu \quad (29)$$

With k_m as the wave vector in the surrounding medium. The final aim of this derivation is to get vector solutions of the wave equations. We begin by

- Transitioning to a spherical coordinate system r, θ, ϕ , since our system is spherically symmetrical
- Defining a scalar function $\psi_{l,m}$

- Defining a constant vector \vec{r}

The scalar function will be a solution of

$$\nabla^2 \psi + k_m^2 \psi = 0 \quad (30)$$

We can construct three vector solutions:

$$\vec{L} = \nabla \psi_{l,m} \quad (31)$$

$$\vec{M}_{l,m} = \nabla \times \vec{r} \psi_{l,m} \quad (32)$$

$$\vec{N}_{l,m} = \frac{1}{k_m} \nabla \times \vec{M}_{l,m} \quad (33)$$

All solutions satisfy the wave equations. $\vec{N}_{l,m}$ and $\vec{M}_{l,m}$ are solenoidal functions and are rotors of each other, like \vec{H} and \vec{E} . \vec{L} , on the other hand is purely longitudinal, so we omit it in this analysis.

A.2 Scalar Solution

In spherical coordinates, the scalar solution, $\psi_{l,m}$ of Equation 30 is a function of R, θ, ϕ

$$\frac{1}{r^2} \frac{\partial}{\partial r} \left(r^2 \frac{\partial \psi}{\partial r} \right) + \frac{1}{r^2 \sin(\theta)} \frac{\partial}{\partial \theta} \left(\sin(\theta) \frac{\partial \psi}{\partial \theta} \right) + \frac{1}{r^2 \sin^2(\theta)} \frac{\partial^2 \psi}{\partial \phi^2} + k_m^2 \psi = 0 \quad (34)$$

Next, we seek a solutions that separates the variables:

$$\psi(r, \theta, \phi) = R(r)\Theta(\theta)\Phi(\phi) \quad (35)$$

Defining constants m, Q , we separate the components into separate solutions:

$$\frac{d^2 \Phi}{d\phi^2} + m^2 \Phi = 0 \quad (36)$$

$$(1 - \cos^2(\theta)) \frac{d^2 \Theta}{d(\cos(\theta))^2} - 2 \cos(\theta) \frac{d\Theta}{d(\cos(\theta))} + \left(Q - \frac{p^2}{1 - \cos^2(\theta)} \right) = 0 \quad (37)$$

$$r^2 \frac{d^2 R}{dr^2} + 2r \frac{dR}{dr} + (k_m^2 r^2 - Q^2) R = 0 \quad (38)$$

The solutions to these equations are as follows:

For Φ

$$\Phi = e^{\pm im\phi} \quad (39)$$

For Θ , representing it as an associated Legendre equation:

$$Q = l(l+1) \rightarrow \quad (40)$$

$$\Theta = P_l^m(\nu) = \frac{(1-\nu^2)^{\frac{m}{2}}}{2^l l!} \frac{d^{l+m}(\nu^2 - 1)^l}{d(\nu)^{l+m}} \quad (41)$$

$$\nu = \cos(\theta) \quad (42)$$

From now on, $P_l^m = P_l^m(\nu)$.

And for R

$$R = \sqrt{\frac{2}{\pi}} Z_l(p) \quad (43)$$

$$p = k_m r \quad (44)$$

Where $Z_l(p)$ represents the radial spherical Bessel $j_l(p)$ or first order Hankel $h_l(p)$. $h_l(p)$, being infinite in the far field are used to represent an outgoing spherical wave pattern for the scattered field. $j_l(p)$ is finite in the origin, so it is a correct representation of incident and transmitted fields.

Combining all of these,

$$\psi_{l,m}(r, \theta, \phi) = \sqrt{\frac{1}{\pi}} Z_l(k_m r) P_l^m e^{im\phi} \quad (45)$$

or, separating into even and odd components:

$$\psi_{l,m,o}(r, \theta, \phi) = \sqrt{\frac{1}{\pi}} Z_l(k_m r) P_l^{m \cos(m\phi)} \quad (46)$$

A.3 Vector Solution

Using the previous equation,

$$\vec{M}_{l,m,o} = \nabla \times \hat{r}(r\psi_{l,m,o}) \quad (47)$$

$$\vec{r} = \hat{r}r \quad (48)$$

By applying the rotor:

$$\vec{M}_{l,m}(\hat{r}) = 0 \quad (49)$$

$$\vec{M}_{l,m,o}^e = \frac{1}{r \sin(\theta)} \frac{d(r\psi)}{d\phi} \hat{\theta} - \frac{1}{r} \frac{d(r\psi)}{d\theta} \hat{\phi} \quad (50)$$

$$= \mp Z_l \frac{P_l^m}{\sin(\theta)} \begin{matrix} \sin \\ \cos \end{matrix}(m\phi) \hat{\theta} - Z_l \frac{dP_l^m}{d\theta} \begin{matrix} \cos \\ \sin \end{matrix}(m\phi) \hat{\phi} \quad (51)$$

And for \vec{N}_{m,l_o^e}

$$\vec{N}_{l,m,o}^e = \frac{l(l+1)}{k_m r} \psi_o^e \hat{r} + \frac{1}{k_m r} \frac{d(r\vec{M}_{l,m,\phi})}{dr} \hat{\theta} + \frac{1}{k_m r} \frac{d(r\vec{M}_{l,m,\theta})}{dr} \hat{\phi} \quad (52)$$

$$= \frac{l(l+1)}{k_m r} Z_l P_l^m \begin{matrix} \cos \\ \sin \end{matrix}(m\phi) \hat{r} + \frac{1}{r} \frac{d(pZ_l)}{dp} \frac{P_l^m}{d\theta} \begin{matrix} \cos \\ \sin \end{matrix} m\phi \hat{\theta} \quad (53)$$

$$\mp m \frac{1}{p} \frac{d(pZ_l)}{dr} \frac{P_l^m}{\sin(\theta)} \begin{matrix} \sin \\ \cos \end{matrix}(m\phi) \hat{\phi} \quad (54)$$

radial p needs to be replaced by Np , $N = \frac{N_s}{N_m}$, which is the relative index of the sphere to the surrounding medium.

A.4 Incident, Scattered and Internal Fields

We assume, that an arbitrary wave, expressed by \vec{A} can be represented by a linear combination of vector functions:

$$\vec{A} = \frac{i}{\omega} \sum_{l,m} \left(A_{l,m} \vec{M}_{l,m} + B_{l,m} \vec{N}_{l,m} \right) \quad (55)$$

Since $\vec{M}_{l,m}$ and $\vec{N}_{l,m}$ are solenoidal function that correspond to interdependence of \vec{H} and \vec{E} , using \vec{A} :

$$\vec{H}_{inc} = \frac{1}{i\omega\mu} \nabla \times \vec{A} \quad (56)$$

$$= -\frac{i}{\omega\mu} \sum \left(A_{l,m} (\nabla \times \vec{M}_{l,m}) + B_{l,m} (\nabla \times \vec{N}_{l,m}) \right) \quad (57)$$

$$= -\frac{ik_m}{\omega\mu} \sum \left(A_{l,m} \vec{N}_{l,m} + B_{l,m} \vec{M}_{l,m} \right) \quad (58)$$

Similarly,

$$\vec{E}_{inc} = \frac{k_m}{\omega^2\epsilon\mu} \sum \left(A_{l,m} \vec{M}_{l,m} + B_{l,m} \vec{N}_{l,m} \right) \quad (59)$$

$A_{l,m}, B_{l,m}$ are expansion coefficients for a particular beam:

$$A_{l,m} = \int M_{l,m}^* \vec{E}_{inc} d\Omega \quad (60)$$

$$B_{l,m} = \int N_{l,m}^* \vec{E}_{inc} d\Omega \quad (61)$$

$$(62)$$

Where $\Omega = 4\pi r$ is the enclosed surface area.

Similarly, the scattered and internal fields can be expanded in terms of $\vec{M}_{l,m}, \vec{N}_{l,m}$:

$$\vec{E}_{scat} = \frac{k_m}{\omega^2 \epsilon \mu} \sum (A_{l,m} a_l \vec{M}_{l,m} + B_{l,m} b_l \vec{N}_{l,m}) \quad (63)$$

$$\vec{H}_{scat} = -\frac{k_m}{\omega \mu} \sum (A_{l,m} a_l \vec{M}_{l,m} + B_{l,m} b_l \vec{N}_{l,m}) \quad (64)$$

$$\vec{E}_{int} = \frac{k_m}{\omega^2 \epsilon_{int} \mu} \sum (A_{l,m} c_l \vec{M}_{l,m} + B_{l,m} d_l \vec{N}_{l,m}) \quad (65)$$

$$\vec{H}_{int} = -\frac{ik_m}{\omega \mu} \sum (A_{l,m} c_l \vec{M}_{l,m} + B_{l,m} d_l \vec{N}_{l,m}) \quad (66)$$

Where a_l, b_l are scattering coefficients and c_d, d_l are internal field coefficients.

A.5 Mie Coefficients

The Mie coefficients a_l, b_l, c_l, d_l can be determined from boundary conditions on the edge of the sphere.

$$(\vec{E}_{inc} + \vec{E}_{scat} - \vec{E}_{int}) \times \vec{r} = 0 \quad (67)$$

$$(\vec{H}_{inc} + \vec{H}_{scat} - \vec{H}_{int}) \times \vec{r} = 0 \quad (68)$$

or,

$$E_{inc,\theta} + E_{scat,\theta} = E_{int,\theta} \quad (69)$$

$$E_{inc,\phi} + E_{scat,\phi} = E_{int,\phi} \quad (70)$$

$$H_{inc,\theta} + H_{scat,\theta} = H_{int,\theta} \quad (71)$$

$$H_{inc,\phi} + H_{scat,\phi} = H_{int,\phi} \quad (72)$$

Which, substituting the vector spherical harmonics, gives:

$$j_l(N\xi)c_l + h_l(\xi)b_l = j_l(\xi) \quad (73)$$

$$[N\xi j_l(N\xi)]'c_l + [\xi h_l(\xi)]'b_l = [\xi j_l(\xi)]' \quad (74)$$

$$Nj_l(N\xi)d_l + h_l(\xi)a_l = j_l(\xi) \quad (75)$$

$$[N\xi j_l(N\xi)]'d_l + N[\xi h_l(\xi)]'a_l = N[\xi j_l(\xi)]' \quad (76)$$

which gives us the standard expressions for the Mie coefficients:

$$a_l = \frac{N^2 j_l(N\xi)[\xi j_l(\xi)]' - j_l(\xi)[N\xi j_l(N\xi)]'}{N^2 j_l(N\xi)[\xi h_l(\xi)]' - h_l(\xi)[N\xi j_l(N\xi)]'} \quad (77)$$

$$b_l = \frac{j_l(N\xi)[\xi j_l(\xi)]' - j_l(\xi)[N\xi j_l(N\xi)]'}{j_l(N\xi)[\xi h_l(\xi)]' - h_l(\xi)[N\xi j_l(N\xi)]'} \quad (78)$$

$$c_l = \frac{j_l(\xi)[\xi h_l(\xi)]' - h_l(\xi)[\xi j_l(\xi)]'}{j_l(N\xi)[\xi h_l(\xi)]' - h_l(\xi)[N\xi j_l(N\xi)]'} \quad (79)$$

$$d_l = \frac{N j_l(\xi)[\xi h_l(\xi)]' - N h_l(\xi)[\xi j_l(\xi)]'}{N^2 j_l(N\xi)[\xi h_l(\xi)]' - h_l(\xi)[N\xi j_l(N\xi)]'} \quad (80)$$

A.6 Cross Sections

Scattering and extinction cross sections can be easily computed, knowing the Mie coefficients.

$$C_{sca} = \frac{W_{sca}}{I_{inc}} \quad (81)$$

$$C_{ext} = \frac{W_{ext}}{I_{inc}} \quad (82)$$

$$W_{sca} = \frac{1}{2} \int_0^{2\pi} \int_0^\pi (E_{sca} \times H_{sca}^*) r^2 \sin(\theta) d\theta d\phi \quad (83)$$

$$= \frac{1}{2} \int_0^{2\pi} \int_0^\pi (E_{sca,\theta} \times H_{sca,\phi}^* - E_{sca,\phi} \times H_{sca,\theta}^*) r^2 \sin(\theta) d\theta d\phi \quad (84)$$

$$W_{ext} = \frac{1}{2} \int_0^{2\pi} \int_0^\pi (E_{inc} \times H_{sca}^*) r^2 \sin(\theta) d\theta d\phi \quad (85)$$

$$= \frac{1}{2} \int_0^{2\pi} \int_0^\pi (E_{inc,\phi} \times H_{sca,\theta}^* - E_{inc,\theta} \times H_{sca,\phi}^* - E_{sca,\phi} \times H_{inc,\theta}^* \\ + E_{sca,\theta} \times H_{inc,\phi}^*) r^2 \sin(\theta) d\theta d\phi \quad (86)$$

Which can be simplified to

$$C_{sca} = \frac{2\pi}{k_m^2} \sum_{l=1}^{\infty} (2l+1)(|a_l|^2 + |b_l|^2) \quad (87)$$

$$C_{ext} = \frac{2\pi}{k_m^2} \Re \sum_{l=1}^{\infty} (2l+1)(a_l + b_l) \quad (88)$$

$$C_{abs} = C_{ext} - C_{sca} \quad (89)$$

Appendix B Raman Scattering from Crystalline Materials

Raman scattering of light from crystalline materials is a versatile method of probing the phonon structure of the materials. A simplistic classical model of Raman scattering is sufficient to demonstrate the effect and to properly predict many of the Raman scattering peaks of semiconductors [30].

We start with an infinite medium with electric susceptibility χ . For simplicity, let us assume that the medium is isotropic and that the susceptibility is scalar. A plane sinusoidal wave is present in the medium, inducing sinusoidal polarization:

$$\vec{F}(\vec{r}, t) = \vec{F}_i(\vec{k}_i, \omega_i) \cos(\vec{k}_i \cdot \vec{r} - \omega_i t) \quad (90)$$

$$\vec{P}(\vec{r}, t) = \vec{P}(\vec{k}_i, \omega_i) \cos(\vec{k}_i \cdot \vec{r} - \omega_i t) \quad (91)$$

$$\vec{P}(\vec{k}_i, \omega_i) = \chi(\vec{k}_i, \omega_i) \vec{F}_i(\vec{k}_i, \omega_i) \quad (92)$$

The lattice has thermal vibrations, quantized into phonons, causing fluctuations in χ . The atomic displacements of a phonon can also be expressed as a plane wave, with wavevector and frequency \vec{q}, ω_0 :

$$\vec{Q}(\vec{r}, t) = \vec{Q}(\vec{q}, \omega_0) \cos(\vec{q} \cdot \vec{r} - \omega_0 t) \quad (93)$$

These phonons will perturb χ . Assuming the characteristic electronic frequencies, which determine χ are much larger than ω_0 , χ can be assumed to be a function of \vec{Q} . At room temperature the amplitudes of the vibrations are small when compared to the lattice constant, meaning we can expand χ as a Taylor series of \vec{Q} :

$$\chi(\vec{k}_i, \omega_i, \vec{Q}) = \chi_0(\vec{k}_i, \omega_i) + \frac{\partial \chi}{\partial \vec{Q}} \Big|_{\vec{Q}=0} \vec{Q}(\vec{r}, t) + \dots \quad (94)$$

where χ_0 is the unperturbed susceptibility and the second term is the effect of the lattice wave. Knowing this, we can express the polarization of the medium with lattice vibrations:

$$\vec{P}(\vec{r}, t, \vec{Q}) = \vec{P}_0(\vec{r}, t) + \vec{P}_{ind}(\vec{r}, t, \vec{Q}) \quad (95)$$

$$\vec{P}_0 = \chi_0(\vec{k}_i, \omega_i) \vec{F}_i(\vec{k}_i, \omega_i) \cos(\vec{k}_i \cdot \vec{r} - \omega_i t) \quad (96)$$

$$\vec{P}_{ind}(\vec{r}, t, \vec{Q}) = \frac{\partial \chi}{\partial \vec{Q}} \Big|_{\vec{Q}=0} \vec{Q}(\vec{r}, t) \vec{F}_i(\vec{k}_i, \omega_i) \cos(\vec{k}_i \cdot \vec{r} - \omega_i t) \quad (97)$$

Such a simplistic description only includes interaction between TO phonons and EM waves, neglecting LO phonons, which can interact with EM waves indirectly, through macroscopic EM fields, but at this moment this is not a serious deficiency.

$$\vec{P}_{ind}(\vec{r}, t, Q) = \frac{\partial \chi}{\partial \vec{Q}_0} \vec{Q}(\vec{q}, \omega_0) \cos(\vec{q} \cdot \vec{r} - \omega_0 t) \\ \times \vec{F}_i(\vec{k}_i, \omega_i) \cos(\vec{k}_i \cdot \vec{r} - \omega_i t) \quad (98)$$

$$= \frac{1}{2} \frac{\partial \chi}{\partial \vec{Q}_0} \vec{Q}(\vec{q}, \omega_0) \vec{F}_i(\vec{k}_i, \omega_i) \\ \cdot \left(\cos((\vec{q} + \vec{k}_i) \cdot \vec{r} + (\omega_0 + \omega_i)t) + \cos((\vec{q} - \vec{k}_i) \cdot \vec{r} + (\omega_0 - \omega_i)t) \right) \quad (99)$$

\vec{P}_{ind} contains two sinusoidal waves - a Stokes shifted ($\omega_S = \omega_0 - \omega_i$, $\vec{k}_S = \vec{k}_i - \vec{q}$) and an anti-Stokes shifted wave ($\omega_A = \omega_0 + \omega_i$, $\vec{k}_A = \vec{k}_i + \vec{q}$). This produces Stokes and anti-Stokes scattered light, with the difference in frequency from the original wave known as the Raman shift.

Since in this case both frequency and wavevector are conserved, single-phonon raman scattering probes only zone-center phonons. Expanding the Taylor series we can easily move to multiple phonon scattering. For two phonon scattering we get combination and difference modes. If the two phonons are identical, then we observe overtone scattering. In this case there is no limit on the wavevector of the individual phonons (only that they need to be identical), meaning that overtone Raman probes the overall phonon density of states.

The intensity of the Raman scattering depends on the polarization of the incident radiation, the scattered radiation and the types of phonons participating in the scattering.

$$I_s \propto |\vec{e}_i \cdot \frac{\partial \chi}{\partial \vec{Q}} \vec{Q}(\omega_0) \cdot \vec{e}_s|^2 \quad (100)$$

This approximates $\vec{q} = 0$ for single phonon scattering. $\frac{\partial \chi}{\partial \vec{Q}}$ is a third-rank tensor with complex components. Introducing $\vec{Q}_n = \vec{Q}/|\vec{Q}|$, a unit vector in the direction of the phonon displacement, we can define a complex second rank tensor,

$$\hat{R} = \frac{\partial \chi}{\partial \vec{Q}} \vec{Q}_n \quad (101)$$

$$I_s \propto |\vec{e}_i \cdot \hat{R} \cdot \vec{e}_s|^2 \quad (102)$$

\hat{R} is the Raman tensor, whose symmetry determines the symmetry of the material's Raman-active phonons. The symmetry of the Raman tensor depends on the symmetry of the medium and the active phonons.

Appendix C Femtosecond Laser Ablation

C.1 Generation of femtosecond laser pulses

Femtosecond laser pulse generation is usually done using chirped pulse amplification. A mode-locked seed laser is used to generate a train of low-power femtosecond pulses, which are then temporally stretched, amplified, compressed and output from the laser system. This is necessary, because the final, compressed femtosecond pulse can have extremely high peak power, which would damage the amplification system [69]. The compression and stretching is done by using dispersion to cause different wavelengths of light to travel different distances. This is usually accomplished using either two prisms and a mirror or two diffraction gratings and a mirror, though, using engineered dispersion in optical fibers is also possible [69].

C.2 Ultrashort-pulse laser ablation

Laser ablation by ultrashort pulses, femto- and picosecond pulses, is a very efficient technique of patterning materials, because the short pulse length minimizes the influence of heat conduction on the ablated volume — keeping the ablation very localized and controlled.

In metals and semiconductors having a large concentration of conduction band electrons, most of the light from the pulse is absorbed by conduction band electrons. The conduction band electrons thermalize within a timeframe of 10fs-1ps, while thermalization between the electrons and the lattice is much slower, on the order of 1 – 100ps, meaning that after the absorption of the laser pulse, we have a non-equilibrium state of a hot electron gas at temperature T_e and a cold lattice at T [58].

The evolution of the temperature of the electron gas and the lattice can be described by the following heat equations:

$$C_e \frac{\partial T_e}{\partial t} = \nabla(\kappa_e \nabla T_e) - \Gamma_{e-ph}(T_e - T) + Q(x_\alpha, t) \quad (103)$$

$$C \frac{\partial T}{\partial t} = \nabla(\kappa \nabla T) + \Gamma_{e-ph}(T_e - T) \quad (104)$$

With C_e, C as the heat capacities of the electron gas and the lattice. For a 1D approximation, the source term can be written as

$$Q(z, t) = \alpha A I(t) \exp(-\alpha z) \quad (105)$$

For femtosecond pulses, heat conduction in within the lattice (first right-hand term of Eq. 104) can be ignored. Because the heat capacity of the electron gas is much smaller than that of the lattice, $C_e \ll C$, the electron gas can be heated to very high transient temperatures.

$$C_e = C_0 T_e, \quad T_e \ll T_{Fermi} \equiv \frac{E_F}{k_B} \quad (106)$$

$$C_0 = \frac{\pi^2 N_e k_B}{2T_F} \quad (107)$$

$$C = const, \quad T > \theta_{Debye} \quad (108)$$

The non-equilibrium thermal conductivity of electrons can be approximated by

$$\kappa_e = \kappa_e(T) \times \frac{T_e}{T} \quad (109)$$

Where $\kappa_e(T)$ is the normal, equilibrium, heat conductivity.

For femtosecond pulses, the characteristic cooling time of the hot electron gas due to energy exchange with the lattice is larger than the pulse duration, $\tau_l \ll \tau_e \equiv \frac{C_e}{\Gamma_{e-ph}}$. For $t \ll \tau_e$ or $\Gamma_{e-ph} T_e \ll \frac{C_e T_e}{t}$, electron-phonon coupling can be ignored. Another reasonable approximation, considering the thermal diffusivity of electrons $D_e = \frac{\kappa_e}{C_e}$, $D_e \tau_l < \alpha^{-2}$, is to ignore heat conduction by electrons. Then Eq. 103 simplifies to:

$$\frac{1}{2} C_0 \frac{\partial T_e^2}{\partial t} = \alpha I_a \exp(-\alpha z) \quad (110)$$

$$T_e(t) = \left(T_0^2 + \frac{2\alpha \phi_a(t)}{C_0} \exp(-\alpha z) \right)^{\frac{1}{2}} \quad (111)$$

$$\phi_a(t) = \int_0^t I_a(t') dt' \quad (112)$$

Where T_0 is the initial temperature.

By the end of the pulse, $t = \tau_l$, we get:

$$T_e(\tau_l) \approx \left(\frac{2\alpha \phi_a}{C_0} \right)^{\frac{1}{2}} \exp \left(-2 \frac{\alpha z}{2} \right) \quad (113)$$

For times $t \geq \tau_l$, Equations 104 and 103, with $Q = 0$ describe the evolution of the two systems. The electron gas then rapidly dumps all the energy to the lattice. Continuing to ignore heat conduction, the lattice temperature:

$$T \approx \frac{\alpha \phi_a}{C} \exp(-\alpha z) \quad (114)$$

$$CT = \int_0^{T_e} C_e(T'_e) dT'_e \quad (115)$$

Significant ablation will occur if $CT \approx \Delta H_v$, where ΔH_v is the transition enthalpy. All of these

approximations hold if $T_e \ll \frac{E_F}{k_B}$. The ablated depth is approximately

$$\Delta h = \frac{1}{\alpha} \ln \frac{\phi}{\phi_{th}} \quad (116)$$

$$\phi_{th} = \frac{\Delta H_v}{\alpha A} \quad (117)$$

This is a very crude approximation, that disregards energy transport by ballistic and diffusive electron propagation; lattice deformation, thermionic electron emission, etc... A more rigorous treatment would include lattice deformations caused by the heated electron gas. The deformation wave caused by the electron gas could cause the metal to fracture and ablate, without significant heating of the lattice itself.

Appendix D Discrete Dipole Approximation

The discrete dipole approximation is a method of numerically simulating light scattering from arbitrarily shaped particles. The general idea of the method is to replace an arbitrarily shaped scatterer by a set of point dipoles and calculate the scattering by each dipole on its one plus the interaction between the dipoles. This makes calculations straightforward for scatterers of arbitrary geometries and compositions.

The following derivation is based on the derivation found in Ref. [31]. For it we assume non-magnetic materials $\mu = 1$ and $e^{-i\omega t}$ time dependence. For simplicity, the dielectric permittivity is assumed to be isotropic, i.e. scalar. Generalization to anisotropic scalars is generally straightforward.

The general form of the integral equation describing the electric field inside the dielectric scatterer can be written as follows:

$$\vec{E}(\vec{r}) = \vec{E}_{inc}(\vec{r}) + \int_{V \setminus V_0} d^3 r' \hat{G}(\vec{r}, \vec{r}') \chi(\vec{r}') \vec{E}(\vec{r}') \\ + \hat{M}(V_0, \vec{r}) - \hat{L}(\partial V_0, \vec{r}) \chi(\vec{r}) \vec{E}(\vec{r}) \quad (118)$$

Where $\vec{E}_{inc}(\vec{r})$ is the incident field, $\vec{E}(\vec{r})$ is the total field at point \vec{r} . $\chi(\vec{r}) = \frac{\epsilon(\vec{r}) - 1}{4\pi}$. V is the total volume, $V_0 \subset V$, $\vec{r} \in V_0 \setminus \partial V_0$.

$\hat{G}(\vec{r}, \vec{r}')$ is the free space dyadic Green's function:

$$\hat{G}(\vec{r}, \vec{r}') = \left(k^2 \hat{I} + \hat{\nabla} \hat{\nabla} \right) \frac{e^{ikR}}{R} \quad (119)$$

$$= \frac{e^{ikR}}{R} \left(k^2 \left(\hat{I} - \frac{\hat{R} \hat{R}}{R^2} \right) - \frac{1 - ikR}{R^2} \left(\hat{I} - 3 \frac{\hat{R} \hat{R}}{R^2} \right) \right) \quad (120)$$

where: $k = \frac{\omega}{c}$, $\vec{R} = \vec{r} - \vec{r}'$, $R = |\vec{R}|$, $\hat{R} \hat{R}$ is a dyadic $\hat{R} \hat{R}_{\mu\nu} = R_\mu R_n u$

\hat{M} is an integral associated with the finite exclusion volume V_0 :

$$\hat{M}(V_0, \vec{r}) = \int_{V_0} d^3 r' \left(\hat{G}(\vec{r}, \vec{r}') \chi(\vec{r}') \vec{E}(\vec{r}') - \hat{G}^s(\vec{r}, \vec{r}') \chi(\vec{r}') \vec{E}(\vec{r}') \right) \quad (121)$$

where $\hat{G}^s(\vec{r}, \vec{r}')$ is the static limit ($k \rightarrow 0$) of $\hat{G}(\vec{r}, \vec{r}')$:

$$\hat{G}^s(\vec{r}, \vec{r}') \chi(\vec{r}') \vec{E}(\vec{r}') = \hat{\nabla} \hat{\nabla} \frac{1}{R} = -\frac{1}{R^3} \left(\hat{I} - 3 \frac{\hat{R} \hat{R}}{R^2} \right) \quad (122)$$

\hat{L} is the self-interaction dyadic:

$$\hat{L}(\partial V_0, vecr) = - \oint_{\partial V_0} d^2 r' \frac{\hat{n}' \hat{R}}{R^3} \quad (123)$$

Where \hat{n}' is an external normal to the surface of V_0 , ∂V_0 at \vec{r}' . \hat{L} is an always real, symmetric dyadic with trace equal to 4π . \hat{L} does not depend on the size of the volume, only on its shape. \hat{M} depends on the size of the volume and approaches 0 when the size of the volume decreases.

The original integral equation is then discretized:

$$V = \bigcup_{i=1}^N V_i \quad (124)$$

$$V_i \cap V_j = 0, i \neq j \quad (125)$$

For simplicity, the volumes are general equal, and in the DDA are called dipoles. Assuming $\vec{r} \in V_i$ and $V_0 = V_i$, the first equation becomes:

$$\begin{aligned} \vec{E}(\vec{r}) &= \vec{E}_{inc}(\vec{r}) + \sum_{j \neq i} \int_{V_j} d^3 r' \hat{G}(\vec{r}, \vec{r}') \chi(\vec{r}') \vec{E}(\vec{r}') \\ &\quad + \hat{M}(V_i, \vec{r}) - \hat{L}(\partial V_i, \vec{r}) \chi(\vec{r}) \vec{E}(\vec{r}) \end{aligned} \quad (126)$$

This sum is exact. Next, we fix \vec{r}_i in each V_i — its center. Then, for $\vec{r} = \vec{r}_i$, we can assume that

$$\int_{V_j} d^3 r' \hat{G}(\vec{r}_i, \vec{r}') \chi(\vec{r}') \vec{E}(\vec{r}') = V_j \hat{G}_{ij} \chi(\vec{r}_j) \vec{E}(\vec{r}_j) \quad (127)$$

$$\hat{M}(V_j, \vec{r}_j) = \hat{M}_i \chi(\vec{r}_i) \vec{E}(\vec{r}_i) \quad (128)$$

meaning that the integrals depend on the values of χ, \vec{E} at \vec{r}_i . Further, the integral equation can be written as

$$\vec{E}_i = \vec{E}_{i,inc} + \sum_{i \neq j} \hat{G}_{ij} V_j \chi_j \vec{E}_j + (\hat{M}_i - \hat{L}_i) \chi_i \vec{E}_i \quad (129)$$

$$\vec{E}_j = \vec{E}(\vec{r}_j) \quad (130)$$

$$\vec{E}_{i,inc} = \vec{E}_{inc}(\vec{r}_j) \quad (131)$$

$$\chi_j = \chi(\vec{r}_j) \quad (132)$$

$$\hat{L}_j = \hat{L}(\partial V_j, \vec{r}_j) \quad (133)$$

Generally, the subvolumes are assumed to be small enough that

$$\vec{E}(\vec{r}) = \vec{E}_i \quad (134)$$

$$\chi(\vec{r}) = \chi_i \quad (135)$$

$$\vec{r} \in V_i \quad (136)$$

meaning that

$$\hat{M}_i^{approx} = \text{int}_{V_i} d^3 r' \left(\hat{G}(\vec{r}_i, \vec{r}') - \hat{G}^s(\vec{r}, \vec{r}') \right) \quad (137)$$

$$\hat{G}_{ij}^{approx} = \frac{1}{V_j} \int_{V_j} d^3 r' \hat{G}(\vec{r}_i, \vec{r}') \quad (138)$$

next we apply a further approximation,

$$\hat{G}_{ij}^{approx} = \hat{G}(\vec{r}_i, \vec{r}_j) \quad (139)$$

This assumption is equivalent to replacing the initial scattering volume by a set of point dipoles. It is possible to formulate the DDA with a weaker set of assumptions, but the greatly increases computational complexity.

The DDA solves for exciting electric fields:

$$\vec{E}_i^{exc} = \left(\hat{I} + (\hat{L}_i - \hat{M}_i) \chi_i \right) \vec{E}_i = \vec{E}_i - \vec{E}_i^{self} \quad (140)$$

$$\vec{E}_i^{self} = (\hat{M}_i - \hat{L}_i) \chi_i \vec{E}_i \quad (141)$$

Where \vec{E}_i^{self} is the field induced by the subvolume on itself. Then the original equation is equivalent to

$$\vec{E}_i^{inc} = \vec{E}_i^{exc} - \sum_{j \neq i} \hat{G}_{ij} \hat{\alpha}_j \vec{E}_j^{exc} \quad (142)$$

where $\hat{\alpha}_i$ is the polarizability tensor:

$$\hat{\alpha}_i = V_i \chi_i \left(\hat{I} + (\hat{L}_i - \hat{M}_i) \chi_i \right)^{-1} \quad (143)$$

An equivalent formulation of the DDA solves for induced polarizations:

$$\vec{P}_i = \hat{\alpha}_i \vec{E}_i^{exc} = V_i \chi_i \vec{E}_i \quad (144)$$

$$\vec{E}_i^{inc} = \hat{\alpha}_i^{-1} \vec{P}_i - \sum_{j \neq i} \hat{G}_{ij} \vec{P}_j \quad (145)$$

This formulation turns out to be preferable for numerical simulations.

Different formulations of the DDA use different approximations for the polarizability tensor $\hat{\alpha}$. The original formulation uses the Clausius-Mossotti polarizability:

$$\hat{\alpha}_i = \hat{I} \alpha_i^{CM} = \hat{I} d^3 \frac{3}{4\pi} \frac{\epsilon_i - 1}{\epsilon_i + 2} \quad (146)$$

After determining the internal field, we can calculate the scattered fields and cross sections of the scatterer. The scattered fields obtained by taking the limit $r \rightarrow \infty$ of the integral in the initial equation, from which all of the DDA was derived:

$$\vec{E}^{sca}(\vec{r}) = \frac{e^{ikr}}{-ikr} \vec{F}(\vec{n}) \quad (147)$$

$$\vec{F}(\vec{n}) = -ik^3 (\hat{I} - \hat{n}\hat{n}) \sum_i \int_{V_i} d^3 r' e^{-ik\vec{r}' \cdot \vec{n}} \chi(\vec{r}') \vec{E}(\vec{r}') \vec{n} = \frac{\vec{r}}{r} \quad (148)$$

Knowing $\vec{F}(\vec{n})$, any other necessary scattering properties can be calculated. E.g. cross sections. For an incident plane wave:

$$\vec{E}^{inc}(\vec{r}) = \vec{e}^0 e^{i\vec{k} \cdot \vec{r}} \quad (149)$$

The scattering cross section, C_{sca} is:

$$C_{sca} = \frac{1}{k^2} \oint d\Omega \left| \vec{F}(\vec{n}) \right|^2 \quad (150)$$

using internal fields, absorption and extinction cross sections:

$$C_{abs} = 4\pi k \sum_i \int_{V_i} d^3 r' \Im(\chi(\vec{r}')) \left| \vec{E}(\vec{r}') \right|^2 \quad (151)$$

$$C_{ext} = 4\pi k \sum_i \int_{V_i} d^3 r' \Im \left(\chi(\vec{r}') \vec{E}(\vec{r}') \cdot (\vec{E}^{inc}(\vec{r}'))^* \right) \quad (152)$$

$$= \frac{4\pi}{k^2} \Re \left(\vec{F} \left(\frac{\vec{k}}{k} \right) \cdot \vec{e}^{0*} \right) \quad (153)$$

These can be expressed in terms of internal fields:

$$C_{abs} = 4\pi k \sum_i V_i \Im(\chi_i) |\vec{E}_i|^2 = 4\pi k \sum_i \Im(\vec{P}_i \vec{E}_i^*) \quad (154)$$

$$C_{ext} = 4\pi k \sum_i \Im(\vec{P}_i \cdot \vec{E}_i^{inc*}) \quad (155)$$

Most errors in the DDA are related to discretization errors, shape errors or the model used to describe the polarizability tensor.

Appendix E Finite Integration Technique

The Finite Integration Technique (FIT) is a method for discretizing the Maxwell equations onto an arbitrary grid [70]. Because the FIT deals with the integral forms of the Maxwell equations, it, Unlike the Finite-Difference Time-Domain (FDTD) methods, does not have any restrictions on the type of grid, other than that it be homeomorphic to a simplicial complex.

For the simplicity of the following derivation [71], we will assume the cells of the grid to be brick shaped. In this case the cell complex can be described as follows:

$$\Omega = [0, L_x] \times [0, L_y] \times [0, L_z] \quad (156)$$

$$\Omega_{c,x} = \{x_i, x_1, \dots, x_m\}, x_i = \frac{L_x - 0}{m} * i \quad (157)$$

$$\Omega_{c,y} = \dots \quad (158)$$

$$\Omega_{c,z} = \dots \quad (159)$$

$$\Omega_{s,x} = \{s_0, s_1, \dots, s_m - 1\}, s_i = \frac{1}{2}(x_i + x_i + 1) \quad (160)$$

$$\Omega_{s,y} = \dots \quad (161)$$

$$\Omega_{s,z} = \dots \quad (162)$$

These can be combined into 8 different three-dimensional grids, combining main (c) and staggered (s) grid points:

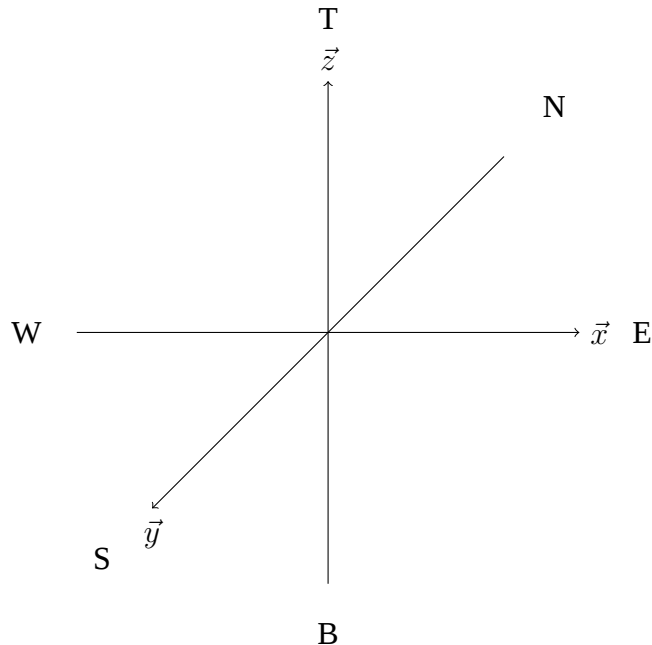


Figure 13: Schematic of used names for sides/directions of the unit cell

$$\Omega_{t_x, t_y, t_z} = \Omega_{t_x} \times \Omega_{t_y} \times \Omega_{t_z} \quad (163)$$

$$t_i = (c, s) \quad (164)$$

The grid is specified by cell size and overall computational domain size. Simplest case is when $h_x = h_y = h_z$, a uniform grid.

$$h_x = \frac{L_x}{m_x} \quad (165)$$

$$h_y = \frac{L_y}{m_y} \quad (166)$$

$$h_z = \frac{L_z}{m_z} \quad (167)$$

$$(168)$$

Discretizing of the Maxwell equations on this set of grids within the framework of the FIT is done starting with the integral form of the equations:

$$\frac{\partial}{\partial t} \int \int_{A_p} \epsilon(\vec{r}) \vec{E}(\vec{r}, t) d\vec{A} = \oint_{\partial A_p} \vec{H}(\vec{r}, t) d\vec{r} - \int \int_{A_p} \sigma(\vec{r}) \vec{E}(\vec{r}, t) d\vec{A} \quad (169)$$

$$\frac{\partial}{\partial t} \int \int_{A_p^*} \mu(\vec{r}) \vec{H}(\vec{r}, t) d\vec{A}^* = - \oint_{\partial A_p^*} \vec{E}(\vec{r}, t) d\vec{r} - \int \int_{A_p^*} \sigma^*(\vec{r}) \vec{H}(\vec{r}, t) d\vec{A}^* \quad (170)$$

(171)

These equations are then discretized on the staggered grid, with electric field calculated on the main grid and magnetic on the staggered one (superscript denotes timestep).

$$\frac{\vec{E}_h^{n+1} - \vec{E}_h^n}{\tau} \int \int_{A_p} \epsilon(\vec{r}) d\vec{A} = \oint_{\partial A_p} \vec{H}_h^{n+\frac{1}{2}}(\vec{r}) d\vec{r} - \vec{E}_h^{n+1} \int \int_{A_p} \sigma(\vec{r}) d\vec{A} \quad (172)$$

$$\frac{\vec{H}_h^{n+\frac{1}{2}} - \vec{H}_h^{n-\frac{1}{2}}}{\tau} \int \int_{A_p^*} \mu(\vec{r}) d\vec{A} = - \oint_{\partial A_p^*} \vec{E}_h^n(\vec{r}) d\vec{r} - \vec{H}_h^{n+\frac{1}{2}} \int \int_{A_p^*} \sigma^*(\vec{r}) d\vec{A}^* \quad (173)$$

Where effective permittivities and conductivities at points other than where they are defined are approximated by averaging the values from the closest available points.

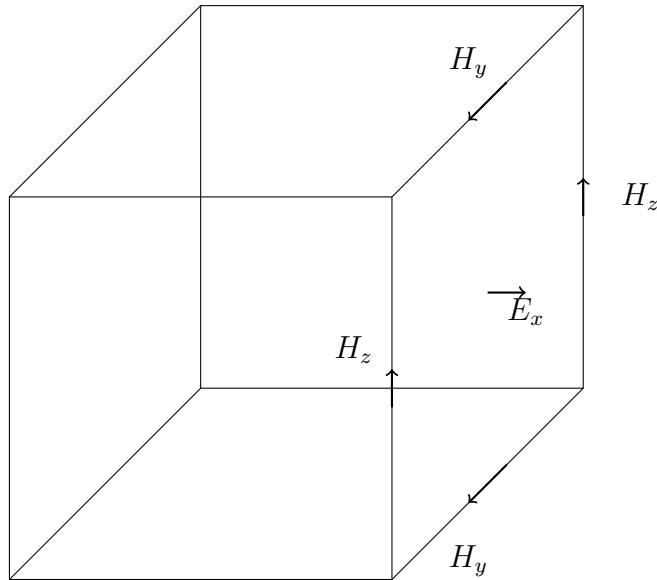


Figure 14: Surface of integration of a cell for E_x component

for the cell depicted in Fig. 14, we have

$$d\vec{A} = \vec{n} dA = \vec{e}_x dy dz \quad (174)$$

$$d\vec{r}_y = \vec{t} dr = \vec{e}_y dy \quad (175)$$

$$d\vec{r}_z = \vec{t} dr = \vec{e}_z dz \quad (176)$$

which means that the above equations simplify to

$$\oint_{\partial A_p} \vec{H}_C^{n+\frac{1}{2}}(\vec{r}) d\vec{r} = \int_{C_1} H_y|_D^{n+\frac{1}{2}} - \int_{C_3} H_y|_T^{n+\frac{1}{2}} dy \quad (177)$$

$$+ \int_{C_2} H_z|_N^{n+\frac{1}{2}} dz - \int_{C_4} H_z|_S^{n+\frac{1}{2}} dz \quad (178)$$

$$= H_y|_D^{n+\frac{1}{2}} \int_{C_1} dy - H_y|_T^{n+\frac{1}{2}} \int_{C_3} dy + H_z|_N^{n+\frac{1}{2}} \int_{C_2} dz - H_z|_S^{n+\frac{1}{2}} \int_{C_4} dz \quad (179)$$

$$= H_y|_D^{n+\frac{1}{2}} \Delta y - H_y|_T^{n+\frac{1}{2}} \Delta y + H_z|_N^{n+\frac{1}{2}} \Delta z - H_z|_S^{n+\frac{1}{2}} \Delta z \quad (180)$$

$$(181)$$

Based on this, the update equations for the components of \vec{E} can be written as:

$$E_x|M^{n+1} = \frac{1}{1 + \tau \frac{\sigma_p}{\epsilon_p}} E_x|M^n + \frac{\frac{\tau}{\sigma_p}}{1 + \tau \frac{\sigma_p}{\epsilon_p}} \left[\frac{H_z|_N^{n+\frac{1}{2}} - H_z|_S^{n+\frac{1}{2}}}{\Delta y} - \frac{H_y|_T^{n+\frac{1}{2}} - H_y|_D^{n+\frac{1}{2}}}{\Delta z} \right] \quad (182)$$

$$E_y|M^{n+1} = \frac{1}{1 + \tau \frac{\sigma_p}{\epsilon_p}} E_y|M^n + \frac{\frac{\tau}{\sigma_p}}{1 + \tau \frac{\sigma_p}{\epsilon_p}} \left[\frac{H_x|_T^{n+\frac{1}{2}} - H_x|_D^{n+\frac{1}{2}}}{\Delta z} - \frac{H_z|_W^{n+\frac{1}{2}} - H_z|_E^{n+\frac{1}{2}}}{\Delta x} \right] \quad (183)$$

$$E_z|M^{n+1} = \frac{1}{1 + \tau \frac{\sigma_p}{\epsilon_p}} E_z|M^n + \frac{\frac{\tau}{\sigma_p}}{1 + \tau \frac{\sigma_p}{\epsilon_p}} \left[\frac{H_y|_W^{n+\frac{1}{2}} - H_y|_E^{n+\frac{1}{2}}}{\Delta x} - \frac{H_x|_N^{n+\frac{1}{2}} - H_x|_S^{n+\frac{1}{2}}}{\Delta y} \right] \quad (184)$$

Using the same method, we can derive the update equations for the components of $vecH$:

$$d\vec{A}^* = \vec{n} dA^* = \vec{e}_x dy dz \quad (185)$$

$$d\vec{R}_y = \vec{t} dr = \vec{e}_y dy \quad (186)$$

$$d\vec{r}_z = \vec{t} dr = \vec{e}_z dz \quad (187)$$

$$\oint_{\partial A_p} \vec{E}_C^n(\vec{r}) d\vec{r} = \int_{C_1} E_y|_T^n dy - \int_{C_3} E_y|_D^n dy - \int_{C_2} E_z|_N^n dz + \int_{C_4} E_z|_S^n dz \quad (188)$$

$$= E_y|_T^n \int_{C_1} dy - E_y|_D^n \int_{C_3} dy - E_z|_N^n \int_{C_2} dz + E_z|_S^n \int_{C_4} dz \quad (189)$$

$$= E_y|_T^n \Delta y - E_y|_D^n \Delta y - E_z|_N^n \Delta z + E_z|_S^n \Delta z \quad (190)$$

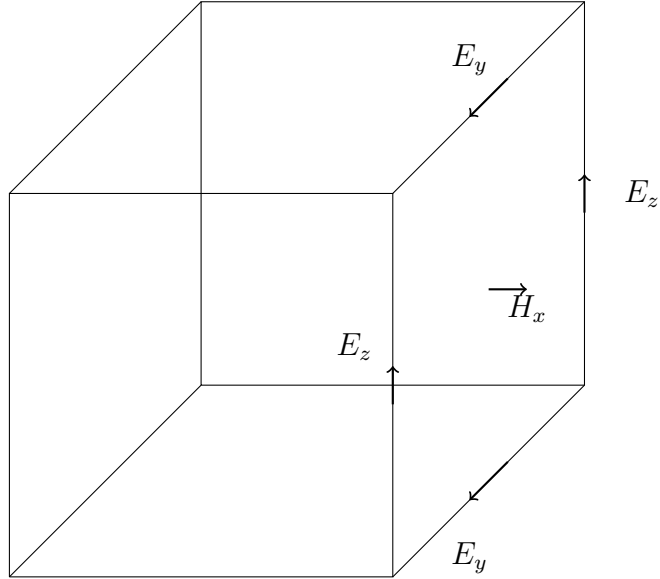


Figure 15: Surface of integration of a cell for H_x component

$$H_x|_M^{n+\frac{1}{2}} = \frac{1}{1 + \tau \frac{\sigma_p^*}{\mu_p}} H_x|_M^{n-\frac{1}{2}} + \frac{\frac{\tau}{\sigma_p^*}}{1 + \tau \frac{\sigma_p^*}{\mu_p}} \left[\frac{E_y|_T^n - E_y|_D^n}{\Delta z} - \frac{E_z|_N^n - E_z|_S^n}{\Delta y} \right] \quad (191)$$

$$H_y|_M^{n+\frac{1}{2}} = \frac{1}{1 + \tau \frac{\sigma_p^*}{\mu_p}} H_y|_M^{n-\frac{1}{2}} + \frac{\frac{\tau}{\sigma_p^*}}{1 + \tau \frac{\sigma_p^*}{\mu_p}} \left[\frac{E_z|_T^n - E_z|_D^n}{\Delta x} - \frac{E_x|_N^n - E_x|_S^n}{\Delta z} \right] \quad (192)$$

$$H_z|_M^{n+\frac{1}{2}} = \frac{1}{1 + \tau \frac{\sigma_p^*}{\mu_p}} H_z|_M^{n-\frac{1}{2}} + \frac{\frac{\tau}{\sigma_p^*}}{1 + \tau \frac{\sigma_p^*}{\mu_p}} \left[\frac{E_x|_T^n - E_x|_D^n}{\Delta y} - \frac{E_y|_N^n - E_y|_S^n}{\Delta x} \right] \quad (193)$$

The main advantage of using FIT over FDTD is that it is not tied the geometry of the grid — it is easier to optimize the geometry of the grid to the geometry that is being studied.

References

1. Krasnok Alexander, Makarov Sergey, Petrov Mikhail et al. Towards all-dielectric metamaterials and nanophotonics // SPIE Optics+ Optoelectronics / International Society for Optics and Photonics. — 2015. — P. 950203–950203.
2. Mie Gustav. Beiträge zur Optik trüber Medien, speziell kolloidaler Metallösungen // Annalen der physik. — 1908. — Vol. 330, no. 3. — P. 377–445.
3. Kuznetsov Arseniy I, Miroshnichenko Andrey E, Fu Yuan Hsing et al. Magnetic light // Scientific reports. — 2012. — Vol. 2.
4. Palik Edward D. Handbook of optical constants of solids. — Academic press, 1998. — Vol. 3.
5. Popa Bogdan-Ioan, Cummer Steven A. Compact dielectric particles as a building block for low-loss magnetic metamaterials // Physical review letters. — 2008. — Vol. 100, no. 20. — P. 207401.
6. Zhao Qian, Zhou Ji, Zhang Fuli, Lippens Didier. Mie resonance-based dielectric metamaterials // Materials Today. — 2009. — Vol. 12, no. 12. — P. 60–69.
7. Evlyukhin Andrey B, Reinhardt Carsten, Seidel Andreas et al. Optical response features of Si-nanoparticle arrays // Physical Review B. — 2010. — Vol. 82, no. 4. — P. 045404.
8. García-Etxarri Aitzol, Gómez-Medina R, Froufe-Pérez Luis S et al. Strong magnetic response of sub-micron silicon particles in the infrared // Optics express. — 2011. — Vol. 19, no. 6. — P. 4815–4826.
9. Krasnok Alexander E, Miroshnichenko Andrey E, Belov Pavel A, Kivshar Yuri S. All-dielectric optical nanoantennas // Optics Express. — 2012. — Vol. 20, no. 18. — P. 20599–20604.
10. Ginn James C, Brener Igal, Peters David W et al. Realizing optical magnetism from dielectric metamaterials // Physical review letters. — 2012. — Vol. 108, no. 9. — P. 097402.
11. Fu Yuan Hsing, Kuznetsov Arseniy I, Miroshnichenko Andrey E et al. Directional visible light scattering by silicon nanoparticles // Physical Review Letters. — 2012.
12. Albelia Pablo, Poyli M Ameen, Schmidt Mikolaj K et al. Low-loss electric and magnetic field-enhanced spectroscopy with subwavelength silicon dimers // The Journal of Physical Chemistry C. — 2013. — Vol. 117, no. 26. — P. 13573–13584.
13. Zambrana-Puyalto Xavier, Bonod Nicolas. Purcell factor of spherical Mie resonators // Physical Review B. — 2015. — Vol. 91, no. 19. — P. 195422.
14. Bakker Reuben M, Permyakov Dmitry, Yu Ye Feng et al. Magnetic and electric hotspots with silicon nanodimers // Nano Letters. — 2015. — Vol. 15, no. 3. — P. 2137–2142.

15. Calderola Martín, Albella Pablo, Cortés Emilio et al. Non-plasmonic nanoantennas for surface enhanced spectroscopies with ultra-low heat conversion // *Nature communications*. — 2015. — Vol. 6.
16. Spinelli P, Verschuuren MA, Polman A. Broadband omnidirectional antireflection coating based on subwavelength surface Mie resonators // *Nature communications*. — 2012. — Vol. 3. — P. 692.
17. Moitra Parikshit, Slovick Brian A, Gang Yu Zhi et al. Experimental demonstration of a broadband all-dielectric metamaterial perfect reflector // *Applied Physics Letters*. — 2014. — Vol. 104, no. 17. — P. 171102.
18. Decker Manuel, Staude Isabelle, Falkner Matthias et al. High-efficiency dielectric Huygens' surfaces // *Advanced Optical Materials*. — 2015. — Vol. 3, no. 6. — P. 813–820.
19. Yu Ye Feng, Zhu Alexander Y, Paniagua-Domínguez Ramón et al. High-transmission dielectric metasurface with 2π phase control at visible wavelengths // *Laser & Photonics Reviews*. — 2015. — Vol. 9, no. 4. — P. 412–418.
20. Krasnok Alexander E, Simovski Constantin R, Belov Pavel A, Kivshar Yuri S. Superdirective dielectric nanoantennas // *Nanoscale*. — 2014. — Vol. 6, no. 13. — P. 7354–7361.
21. Krasnok Alexander E, Filonov Dmitry S, Simovski Constantin R et al. Experimental demonstration of superdirective dielectric antenna // *Applied Physics Letters*. — 2014. — Vol. 104, no. 13. — P. 133502.
22. Shcherbakov Maxim R, Neshev Dragomir N, Hopkins Ben et al. Enhanced third-harmonic generation in silicon nanoparticles driven by magnetic response // *Nano letters*. — 2014. — Vol. 14, no. 11. — P. 6488–6492.
23. Makarov Sergey, Kudryashov Sergey, Mukhin Ivan et al. Tuning of magnetic optical response in a dielectric nanoparticle by ultrafast photoexcitation of dense electron–hole plasma // *Nano letters*. — 2015. — Vol. 15, no. 9. — P. 6187–6192.
24. Li HH. Refractive index of silicon and germanium and its wavelength and temperature derivatives // *Journal of Physical and Chemical Reference Data*. — 1980. — Vol. 9, no. 3. — P. 561–658.
25. Dmitriev Pavel A, Baranov Denis G, Milichko Valentin A et al. Resonant Raman scattering from silicon nanoparticles enhanced by magnetic response // *Nanoscale*. — 2016. — Vol. 8, no. 18. — P. 9721–9726.
26. Hayes William, Loudon Rodney. Scattering of light by crystals. — Courier Corporation, 2012.
27. Moskovits Martin. Surface-enhanced spectroscopy // *Reviews of modern physics*. — 1985. — Vol. 57, no. 3. — P. 783.

28. Islam Mohammed N, De Wilde Carl, Kuditcher Amos. Wideband raman amplifiers // Raman Amplifiers for Telecommunications 2. — Springer, 2004. — P. 445–490.
29. Pask H Ml. The design and operation of solid-state Raman lasers // Progress in Quantum Electronics. — 2003. — Vol. 27, no. 1. — P. 3–56.
30. Peter YU, Cardona Manuel. Fundamentals of semiconductors: physics and materials properties. — Springer Science & Business Media, 2010.
31. Yurkin Maxim A, Hoekstra Alfons G. The discrete dipole approximation: an overview and recent developments // Journal of Quantitative Spectroscopy and Radiative Transfer. — 2007. — Vol. 106, no. 1. — P. 558–589.
32. Courant Richard. Variational methods for the solution of problems of equilibrium and vibrations // Lecture Notes in Pure and Applied Mathematics. — 1994. — P. 1–1.
33. Yee Kane. Numerical solution of initial boundary value problems involving Maxwell's equations in isotropic media // IEEE Transactions on antennas and propagation. — 1966. — Vol. 14, no. 3. — P. 302–307.
34. Wieland T. A discretization method for the solution of Maxwell's equations for six-components fields // Electronics and Communications AEU. — 1977. — Vol. 31, no. 3. — P. 116–120.
35. Shi Lei, Tuzer T Umut, Fenollosa Roberto, Meseguer Francisco. A New Dielectric Metamaterial Building Block with a Strong Magnetic Response in the Sub-1.5-Micrometer Region: Silicon Colloid Nanocavities // Advanced materials. — 2012. — Vol. 24, no. 44. — P. 5934–5938.
36. Abbarchi Marco, Naffouti Meher, Vial Benjamin et al. Wafer scale formation of monocrystalline silicon-based mie resonators via silicon-on-insulator dewetting // ACS nano. — 2014. — Vol. 8, no. 11. — P. 11181–11190.
37. Zywiertz Urs, Evlyukhin Andrey B, Reinhardt Carsten, Chichkov Boris N. Laser printing of silicon nanoparticles with resonant optical electric and magnetic responses // Nature communications. — 2014. — Vol. 5.
38. Shi Lei, Harris Justin T, Fenollosa Roberto et al. Monodisperse silicon nanocavities and photonic crystals with magnetic response in the optical region // Nature communications. — 2013. — Vol. 4. — P. 1904.
39. Makarov Sergey V, Milichko Valentin A, Mukhin Ivan S et al. Controllable femtosecond laser-induced dewetting for plasmonic applications // Laser & Photonics Reviews. — 2016. — Vol. 10, no. 1. — P. 91–99.

40. Dmitriev PA, Makarov SV, Milichko VA et al. Direct Femtosecond Laser Writing of Optical Nanoresonators // Journal of Physics: Conference Series / IOP Publishing. — Vol. 690. — 2016. — P. 012021.
41. Thompson Carl V. Solid-state dewetting of thin films // Annual Review of Materials Research. — 2012. — Vol. 42. — P. 399–434.
42. Liu JM. Simple technique for measurements of pulsed Gaussian-beam spot sizes // Optics letters. — 1982. — Vol. 7, no. 5. — P. 196–198.
43. Permyakov Dmitry, Sinev Ivan, Markovich Dmitry et al. Probing magnetic and electric optical responses of silicon nanoparticles // Applied Physics Letters. — 2015. — Vol. 106, no. 17. — P. 171110.
44. Cançado Luiz Gustavo, Beams Ryan, Jorio Ado, Novotny Lukas. Theory of spatial coherence in near-field Raman scattering // Physical Review X. — 2014. — Vol. 4, no. 3. — P. 031054.
45. Murphy DV, Brueck SRJ. Enhanced Raman scattering from silicon microstructures // Optics letters. — 1983. — Vol. 8, no. 9. — P. 494–496.
46. Bohren Craig F, Huffman Donald R. Absorption and scattering by a sphere // Absorption and Scattering of Light by Small Particles. — 1983. — P. 82–129.
47. Ralston JM, Chang RK. Spontaneous-Raman-scattering efficiency and stimulated scattering in silicon // Physical Review B. — 1970. — Vol. 2, no. 6. — P. 1858.
48. Ishimaru Akira. Electromagnetic wave propagation, radiation, and scattering. — Prentice-Hall, 1991.
49. Checoury X, Han Z, El Kurdi M, Boucaud P. Deterministic measurement of the Purcell factor in microcavities through Raman emission // Physical Review A. — 2010. — Vol. 81, no. 3. — P. 033832.
50. Lai HM, Lam CC, Leung Peter T, Young Kenneth. Effect of perturbations on the widths of narrow morphology-dependent resonances in Mie scattering // JOSA B. — 1991. — Vol. 8, no. 9. — P. 1962–1973.
51. Loke Vincent LY, Mengüç M Pinar, Nieminen Timo A. Discrete-dipole approximation with surface interaction: Computational toolbox for MATLAB // Journal of Quantitative Spectroscopy and Radiative Transfer. — 2011. — Vol. 112, no. 11. — P. 1711–1725.
52. Campbell IH, Fauchet Ph M. The effects of microcrystal size and shape on the one phonon Raman spectra of crystalline semiconductors // Solid State Communications. — 1986. — Vol. 58, no. 10. — P. 739–741.
53. De Wolf Ingrid. Micro-Raman spectroscopy to study local mechanical stress in silicon integrated circuits // Semiconductor Science and Technology. — 1996. — Vol. 11, no. 2. — P. 139.

54. Zywietz Urs, Reinhardt Carsten, Evlyukhin Andrey B et al. Generation and patterning of Si nanoparticles by femtosecond laser pulses // *Applied Physics A*. — 2014. — Vol. 114, no. 1. — P. 45–50.
55. Ionin AA, Kudryashov SI, Seleznev LV et al. Thermal melting and ablation of silicon by femtosecond laser radiation // *Journal of Experimental and Theoretical Physics*. — 2013. — Vol. 116, no. 3. — P. 347–362.
56. Wu Chengping, Zhigilei Leonid V. Microscopic mechanisms of laser spallation and ablation of metal targets from large-scale molecular dynamics simulations // *Applied Physics A*. — 2014. — Vol. 114, no. 1. — P. 11–32.
57. Papageorgiou Demetrios T. On the breakup of viscous liquid threads // *Physics of Fluids*. — 1995. — Vol. 7, no. 7. — P. 1529–1544.
58. Bäuerle Dieter W. *Laser processing and chemistry*. — Springer Science & Business Media, 2013.
59. Bulgakova NM, Bulgakov AV. Pulsed laser ablation of solids: transition from normal vaporization to phase explosion // *Applied Physics A: Materials Science & Processing*. — 2001. — Vol. 73, no. 2. — P. 199–208.
60. Itina Tatiana E. Molecular dynamics study of the role of material properties on nanoparticles formed by rapid expansion of a heated target // *Applied Surface Science*. — 2009. — Vol. 255, no. 10. — P. 5107–5111.
61. Amoruso S, Bruzzese R, Spinelli N et al. Generation of silicon nanoparticles via femtosecond laser ablation in vacuum // *Applied Physics Letters*. — 2004. — Vol. 84, no. 22. — P. 4502–4504.
62. Tull BR, Carey JE, Sheehy MA et al. Formation of silicon nanoparticles and web-like aggregates by femtosecond laser ablation in a background gas // *Applied Physics A: Materials Science & Processing*. — 2006. — Vol. 83, no. 3. — P. 341–346.
63. Vuye G, Fisson S, Van V Nguyen et al. Temperature dependence of the dielectric function of silicon using in situ spectroscopic ellipsometry // *Thin Solid Films*. — 1993. — Vol. 233, no. 1-2. — P. 166–170.
64. Zywietz Urs, Schmidt Mikolaj K, Evlyukhin Andrey B et al. Electromagnetic resonances of silicon nanoparticle dimers in the visible // *ACS Photonics*. — 2015. — Vol. 2, no. 7. — P. 913–920.
65. Dmitriev PA, Makarov SV, Milichko VA et al. Laser fabrication of crystalline silicon nanoresonators from an amorphous film for low-loss all-dielectric nanophotonics // *Nanoscale*. — 2016. — Vol. 8, no. 9. — P. 5043–5048.
66. Miroshnichenko Andrey E, Evlyukhin Andrey B, Kivshar Yuri S, Chichkov Boris N. Substrate-induced resonant magnetoelectric effects for dielectric nanoparticles // *ACS Photonics*. — 2015. — Vol. 2, no. 10. — P. 1423–1428.

67. Morita M, Ohmi T, Hasegawa E et al. Growth of native oxide on a silicon surface // Journal of Applied Physics. — 1990. — Vol. 68, no. 3. — P. 1272–1281.
68. Ng Li Na. Manipulation of particles on optical waveguides : Ph. D. thesis / Li Na Ng ; University of Southampton, Faculty of Engineering and Applied Science. — 2000.
69. Harilal Sivanandan S, Freeman Justin R, Diwakar Prasoon K, Hassanein Ahmed. Femtosecond laser ablation: Fundamentals and applications // Laser-Induced Breakdown Spectroscopy. — Springer, 2014. — P. 143–166.
70. Weiland M Clemens T. Discrete electromagnetism with the finite integration technique // Progress In Electromagnetics Research. — 2001. — Vol. 32. — P. 65–87.
71. Rahimi Zhabiz. The Finite Integration Technique (FIT) and the Application in Lithography Simulations : Ph. D. thesis / Zhabiz Rahimi ; Technischen Fakultät der Universität Erlangen-Nürnberg. — 2011.